# Chapter 7
# Utility of 3-D Seismic Attribute Analysis and VSP for Assessing Potential Carbon Sequestration Targets on the Rock Springs Uplift, Southwest Wyoming

**Yuri Ganshin and Ronald C. Surdam**

**Abstract** One of the most important steps in characterizing a geologic $CO_2$ storage site is the construction of 3-D volumes of seismic attributes. Once these seismic attribute volumes are constructed, key attributes can be correlated to core and well-log observations and analytical measurements. These correlations allow standardizations and extrapolations of a variety of determinative rock/fluid characteristics from the well bore of the stratigraphic test well out into the 3-D seismic survey volume, creating a realistic 3-D model of storage reservoirs and seals. This chapter discusses the technique for performing the tasks required to make the seismic attribute volumes; the correlations between key rock/fluid parameters and seismic attributes; and the crucial extrapolations from 1-D core, log, and VSP observations out into 3-D seismic attribute space. Topics covered include surface seismic specifications, seismic data processing, seismic resolution, vertical seismic profiling (VSP) and data acquisition, comparison of VSP and surface seismic data, comparision of VSP and well data (geologic property modeling), horizon mapping and depth conversion, seismic attributes, seismic interpretation, and qualitative permeability determined from seismic attribute analysis.

## 7.1 Introduction

This study began with a year devoted to seismic data conditioning for reflected compressional wave (P-wave) analysis and seismic attribute computation. A 25-square-mile 3-D seismic dataset was processed through pre-stack time migration (PSTM) at Geokinetics and through further processing at the Carbon Management Institute at the University of Wyoming. Automatic velocity analyses were applied at each

---

Y. Ganshin (✉) · R. C. Surdam
Carbon Management Institute Laramie, University of Wyoming, Laramie, USA
e-mail: yganshin@uwyo.edu

R. C. Surdam
e-mail: rsurdam@uwyo.edu

R. C. Surdam (ed.), *Geological $CO_2$ Storage Characterization,*
Springer Environmental Science and Engineering, DOI 10.1007/978-1-4614-5788-6_7,

common-depth-point (CDP) location and resulted in a high-density interval-velocity volume. This velocity volume served as the basis for 3-D geologic modeling and the time-to-depth transformation of the seismic attributes. We computed multiple morphological and physical seismic attributes for the whole seismic volume: among possible attributes we estimated and analyzed were instantaneous and RMS amplitude, instantaneous and mean frequency, spectrally decomposed amplitudes, coherency and curvature, dip azimuth and dip magnitude, velocity, and acoustic impedance.

Petrophysical analysis of wireline well logs allowed us to identify different lithologic types (e.g., sandstones, shales, dolostones) and the corresponding grain matrix properties (density and P-wave velocity) for pre-Cretaceous strata in the RSU #1 well. On the bases of the strong porosity-velocity correlations established for the major sandstone and carbonate reservoir rocks, we were then able to use seismically derived velocities in building porosity distribution models.

We then turned to the characterization of the Mississippian Madison Limestone and its confining layers. To gain more information on regional heterogeneity, we performed multiresolution spectral decomposition analysis of 3-D seismic data. Several domains with diverse seismically derived properties were identified within the reservoir rocks. These domains possibly reveal different tectonic or sequence stratigraphic features. To date, sparse well control within the study area has precluded geologic verification of these seismically defined domains. There are 34 deep wells in the seismic project area, some with well-log and core data available. However, only one of these wells, the RSU #1, penetrates the targeted deep saline aquifers.

Our specific objective was to apply selected seismic attributes to aid in quantifying the reservoir properties and lateral continuity of $CO_2$ sequestration targets. We systematically tested more than a dozen seismic attributes and found that curvature, interval velocity, acoustic impedance, iso-frequency amplitude, and mean frequency were particularly useful in mapping structural trends, performing seismic facies analysis, and imaging porosity distributions within the target horizons. A one-dimensional geologic-property model was developed for the target interval (10,500–12,700 ft (3,200–3,870 m) below KB (kelly bushing) at the RSU #1 well). The model is based on petrographic core facies determinations and petrophysical relationships, and is consistent with VSP observations through synthetic trace modeling. The geologic property model yields estimates of reservoir thickness, porosity, and permeability.

Depth-converted impedance slices show similarity and consistency that suggest that impedance can be useful as a guide for propagating porosity and permeability throughout the 3-D model. Seismic impedance inversion is an inherently underconstrained problem that does not allow the use of rigorous joint inversion methods. In the absence of a true inverse, a unique and reliable solution can be obtained by defining a set of physical constraints that must be satisfied by the resulting images. In this study we used a method for constructing a "synthetic log" volume that is free of subjectively selected user parameters and utilizes the automatically computed, high-density interval velocity volume that can be directly compared to a recorded sonic log. A comparison of synthetic log sections and horizon maps with the conventional seismic data from which they were derived clearly demonstrates improved resolution and understanding of the subsurface geology. This allows re-mapping into porosity units those stratigraphic intervals that are not affected by significant lithologic variation and are characterized by strong velocity-porosity correlation. The resulting porosity maps for the deep saline aquifers are reasonable; however, their accuracy has not been tested, due to sparse well control.

Permeability and porosity are key parameters in reservoir flow simulation. When an impedance-porosity transform is available (as for the Weber Sandstone and Madison Limestone units), porosity can be inferred from acoustic impedance. However, the permeability that necessarily has to be supplied in reservoir modeling seems to be the most elusive of reservoir properties and remains extremely uncertain. In this study, we used a spectral decomposition technique to derive a relative qualitative attribute from seismic data. Based on theoretical predictions for vuggy, dual-porosity carbonate rocks, the normal-incident P-wave reflection should produce low-frequency amplitude resonance for highly permeable reservoir rocks. Correspondingly, we have designed a permeability attribute that is proportional to the difference between the low-frequency spectral amplitude component along the middle Madison reflection horizon and the high-frequency component, and is scaled by the sum of the two components. The resultant permeability attribute maps reveal an extended area of increased permeability south and southwest of the RSU #1 well.

## 7.2 Surface Seismic Specifications

The Jim Bridger 3-D and 3-C is a wide-azimuth seismic data set acquired in Sweetwater County, southwestern Wyoming, using vibroseis as a source and three- component digital sensors covering an area of about 25 $mi^2$. The survey was designed as a baseline study for possible $CO_2$ injection and was acquired by Geokinetics Service Co., Houston, Texas, during November 2010. The cross-spread shooting method used for data acquisition implies multiple perpendicular source and receiver lines (Fig. 7.1). The fold of stack obtainable by this method is relatively high and uniform (averages 30× after CMP binning). However, orthogonal shooting tends to create a non-uniform distribution of offsets, a pattern that is not related to geologic variations and may “leak” into the data, creating an artificial *acquisition footprint*. Regularly oriented gaps in the source and receiver lines due to surface conditions (power plant, ponds, cliffs, roads) (Fig. 7.1) may also introduce acquisition artifacts into the data.

The CMP bin, 110 ft in both the X and Y directions, is less than one-quarter the minimum wavelength ($\lambda_{min} = 500$ ft) and ensures that the data is not spatially biased. The final CMP fold map, Fig. 7.2a, shows a maximum fold of 48× at the center of the survey. The middle part of the survey area is characterized by a maximum offset (source-to-farthest-receiver distance) of 19,800 ft, which is adequate for imaging geologic targets in 10,000–15,000 ft depth range. CMP fold coverage and source-to-receiver offset distributions are the most important survey design parameters that affect reflected signal strength and allow lithology/fluid predictions to be made. A rectangular area (3×3 mi)

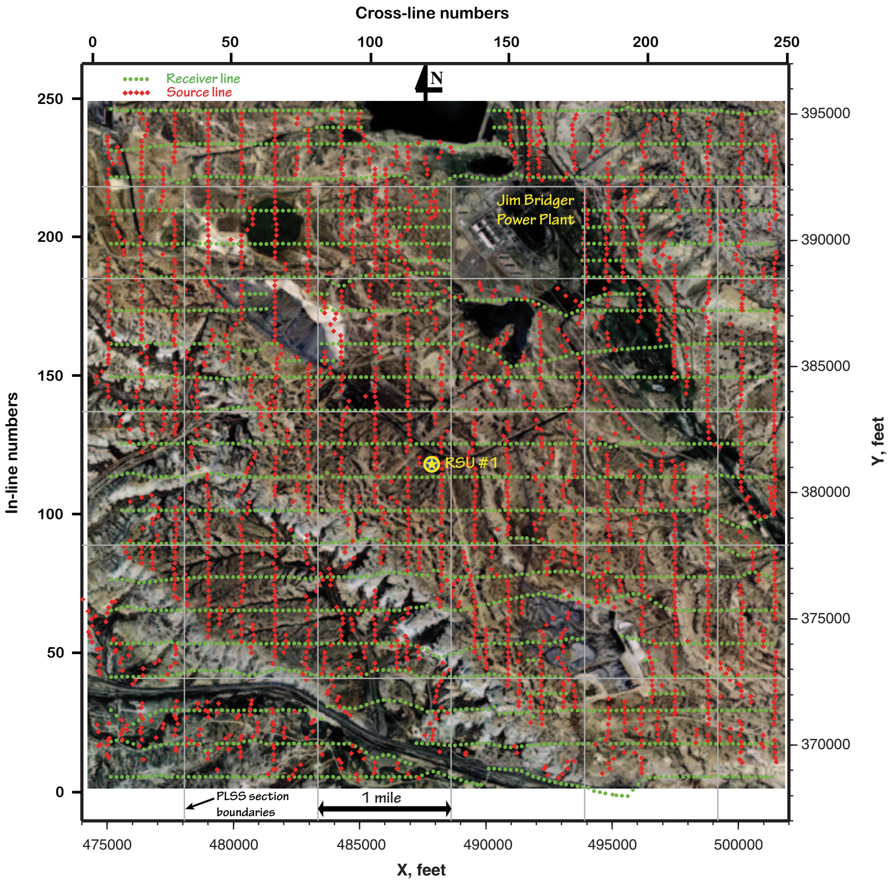

**Fig. 7.1** Jim Bridger 3-D seismic survey. (Source (shotpoint) and receiver layout overlying infrared satellite image)

centered on the RSU #1 well is shown in Fig. 7.2b. This area is characterized by the maximum and most uniform CMP-fold and maximum-offset distributions, enabling the most favorable conditions for seismic imaging of the subsurface geology. The work presented here will concern only compressional (P-wave) data recorded on the vertical component. Table 7.1 summarizes the survey design details.

## 7.3 Seismic Data Preprocessing

Geokinetics did the basic preprocessing of the reflection seismic data. The purpose of data preprocessing was twofold, (1) pre-stack data conditioning for an automated, high-density velocity analyses on CMP gathers and (2) stacked amplitude volume preparation that is suitable for volumetric and horizon attribute analyses. The processing flow used by the Geokinetics processing team is summarized in Table 7.2.

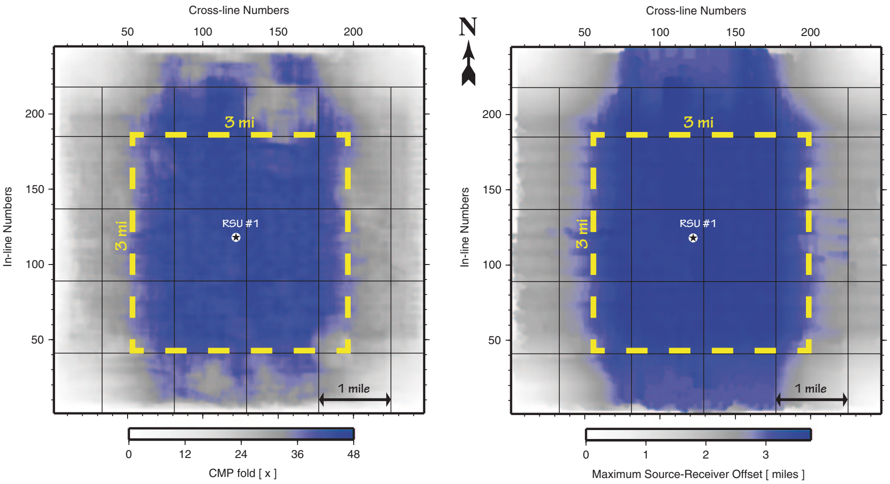

**Fig. 7.2** Jim Bridger 3-D seismic survey. (**a**) CMP fold coverage map and (**b**) maximum source-receiver offset map. The dashed rectangle (3×3 mi) centered around the RSU #1 well, outlines seismic image area where the data is most reliable

The quality of the resultant PSTM stacked amplitude volume is illustrated in Fig. 7.3. Strong and coherent reflections in the time range 1.4–2.2 s correspond to geologic interfaces in the depth range approximately from 7,000 to 13,000 ft below the ground surface at the RSU #1 well location. This means that the structure of the targeted reservoir and sealing stratigraphic units can be imaged with the reflected P-waves. However, an isochrone slice at 2.08 s two-way travel time (horizontal section, Fig. 7.3) clearly demonstrates the acquisition footprint (grid of east-west and north-south stripes) present in the stacked amplitude volume. The theory of Kirchhoff migration assumes that the input data are regularly sampled in X, Y, and offset so that the resulting wavefield can be correctly reconstructed during imaging. If we have a gap in the input, there will be an amplitude anomaly in the output proportional to the gap size. As is seen in Fig. 7.3, the acquisition footprint intensifies northeast from the test well, in the areas with the largest gaps in the shooting scheme (Fig. 7.1). Especially, the seismic data quality deteriorates in the areas corresponding to rough topography and the power plant facilities. Obviously, the footprint removal routine of the Geokinetics processing flow (Step 32) (Table 7.2) didn't do the job completely, thus leaving a potential problem for the subsequent data processing.

## 7.4 Seismic Resolution

Seismic resolution refers to the level of detail that can be seen in seismic data (sections and maps); it is commonly defined as the ability to distinguish separate features. In reflection seismology, the "measuring unit" is the wavelength (λ). Vertical resolution is approximately the one-quarter wavelength λ/4, while lateral resolution is commonly considered to be the larger of the half-wavelength λ/2 or the bin size

**Table 7.1** Survey acquisition details

| | |
|---|---|
| Record length; Sample rate | 6 s, 2 ms |
| Geophone type | SVSM 3-component digital sensor |
| Total geophone stations | 2,514 |
| Total source points | 2,541 |
| Number of live receiver lines | 8 (144 live stations per line) |
| Receiver group and source interval | 220 ft |
| Receiver and source line spacing | 1,320 ft |
| Maximum source to receiver offset | 19,800 ft |
| X, Y coordinate projection | NAD 27, Clarke 1866 |
| X, Y coordinate state plane | Wyoming West Central |
| Survey size | 25.16 $mi^2$ |
| Source type | I/O AVH IV Vibroseis, 4 over flag |
| Sweep parameters | Linear 6–110 Hz |
| Sweep tapers | Linear 300–300 ms |

(110 ft in our survey). In order for two close reflective interfaces to be clearly distinguished, they have to be about one-quarter wavelength apart (Rayleigh Criterion for vertical resolution). Lateral resolution on migrated volumes is difficult to quantify because it depends on many factors, especially the presence of noise. The half-wavelength criterion originates from the sampling theorem that at least two samples per apparent wavelength must be obtained in order to recognize separate features.

Wavelength is obtained from the relationship $\lambda = v/f$, where v is velocity and f is seismic frequency. In the context of our study, the velocity is the compressional wave (P-wave) speed in the vicinity of the target level, which we take as the Weber through Madison interval (2.0–2.2 s on the seismic time sections). As is common in reflection seismology, we use the weighted mean spectral frequency as revealed by continuous Fourier analysis. The dominant seismic frequency in the RSU #1 well vicinity at the target level averages 30 Hz (Fig. 7.4). We take this value as a good representation of the dominant frequency in the entire target area. The average velocity (estimated from smoothed sonic log and detailed seismic interval velocity analysis) of the Weber through Madison section at RSU #1 is about 18,000 ft/s, giving a dominant wavelength of 600 ft. Thus the *vertical resolution* is 150 ft, and the *lateral resolution* is 300 ft. The following assumptions apply to the use of these values: (1) a seismic signal has constant frequency, (2) seismic waves propagate at constant velocity, and (3) the level of background seismic noise is negligible.

## 7.5 Vertical Seismic Profiling (VSP)

A Vertical Seismic Profile is generated by a seismic energy source located at the surface and receivers lowered into a borehole. This type of survey enables calibration of surface seismic data recorded in time-domain to the borehole geology directly, since in VSP we know both *depth* and *time* to seismic reflections. With VSP, geoscientists can rely on accurate, detailed physical measurements rather than on assumptions, predictions, speculations, or synthetic calculations.

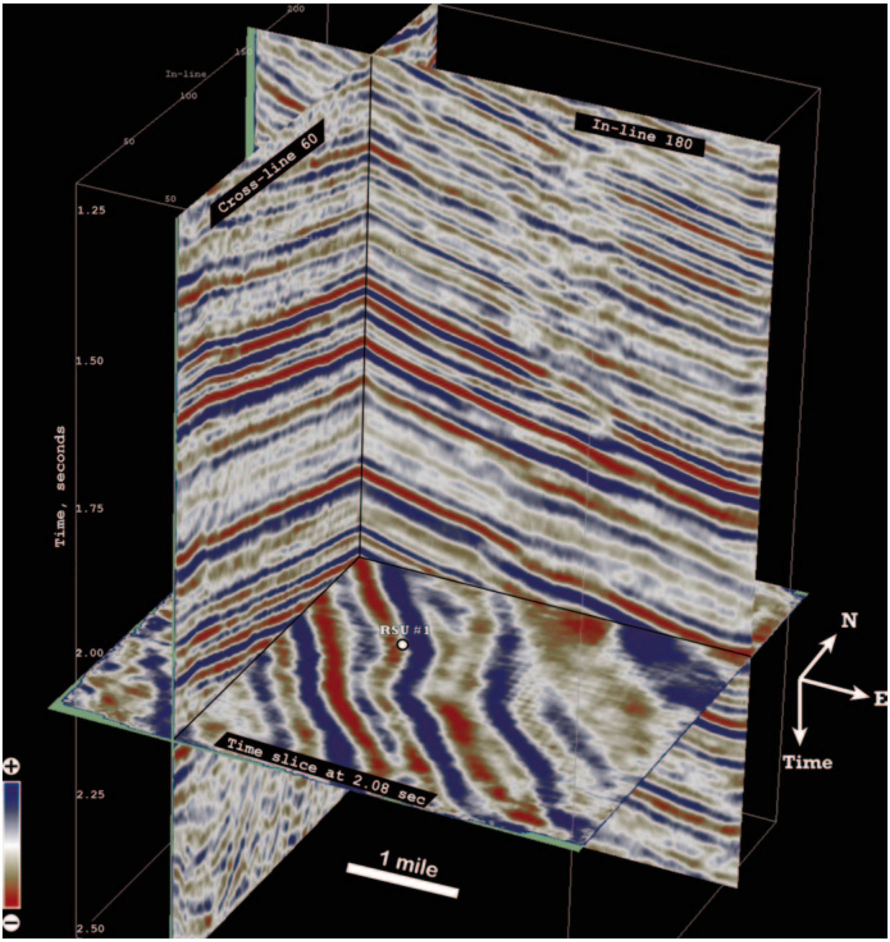

**Fig. 7.3** 3-D seismic amplitude volume displayed in three orthogonal slices. Note an overall northeast dip of reflectors and acquisition footprint pattern in the time slice (regular grid of stripes trending south-north and east-west). Projection of the RSU #1 well location on the time slice is shown approximately

### *7.5.1 VSP Data Acquisition*

Baker Hughes, Inc., Houston, Texas, conducted a zero-offset VSP in the RSU #1 well. The objectives of the VSP Survey were to:

- provide time-depth information and subsurface velocity function.
- generate VSP corridor stack to tie vertical seismic with the 3-D surface seismic.

At the time of the survey, the well was drilled to a depth of 12,810 ft and was cased to 9,750 ft. All measured depths are referenced to the kelly bushing (KB) elevation of 6,860 ft above Mean Sea Level (MSL). The ground elevation at the wellhead is

**Table 7.2** Processing flow (Geokinetics Service Company)

1. Reformat field records to internal Geokinetics format
2. Geometry application, trace edits, and 3-D grid application
3. Convert data to minimum phase
4. Refraction statics analysis and application
5. Spherical divergence correction (true amplitude recovery)
6. Surface consistent gain correction
7. Noise removal and attenuation (MBNA for deconvolution analysis only)
8. Surface consistent deconvolution
9. Noise removal and attenuation (MBNA)
10. First pass velocity analysis (1×1-mi interval)
11. Surface consistent residual statics, first pass
12. Second pass velocity analysis (0.5×0.5-mi interval)
13. Surface consistent residual statics, second pass
14. Accelerometer Integration
15. Noise removal and attenuation (MBNA)
16. Surface consistent residual statics, third pass
17. Mute analysis
18. Post-stack migration
19. Preparation for PSTM (pre-stack time migration): Common offset bin analysis
20. Preparation for PSTM: Sort to common offset bins
21. Preparation for PSTM: Common offset noise attenuation (FXY deconvolution)
22. Preparation for PSTM: Optimize common offset trace population
23. PSTM on select target lines for migration velocity analysis
24. PSTM velocity analysis (0.5×0.5-mi interval)
25. PSTM on entire 3-D volume using smoothed migration velocity from step 24. Kirchhoff algorithm was used on each common offset gather with the following parameters: 110 ft×110 ft output grid size, 60° migrated dip limit, 30,000-ft migration aperture limit (diameter)
26. Common offset noise attenuation (FXY deconvolution)
27. Sort to CMP
28. Residual velocity analysis (0.5×0.5-mi-interval)
29. CMP noise removal and attenuation (MBNA)
30. CMP trim statics
31. Apply NMO, mute, and stack
32. Footprint removal
33. Post stack noise attenuation
34. Time variant band-pass frequency filter (1500–2500 ms → 6–12–60–70 Hz)

6,841.2 ft above MSL. The source used for the VSP survey was two LRS-315 seismic vibrators positioned 285 ft from the wellhead at 6,837 ft elevation above MSL. A 12-s, linear upsweep, with 8–80 Hz frequency range was used for seismic wave generation. A two-level, three-component ASR receiver tool was used to record the seismic wavefield. The depth range of recording was 500–12,800 ft below KB. Data was gathered at 76 down-hole receiver stations. There were 360 files recorded during the survey. The time length of the correlated output data was 6 s with a 2 ms sampling rate.

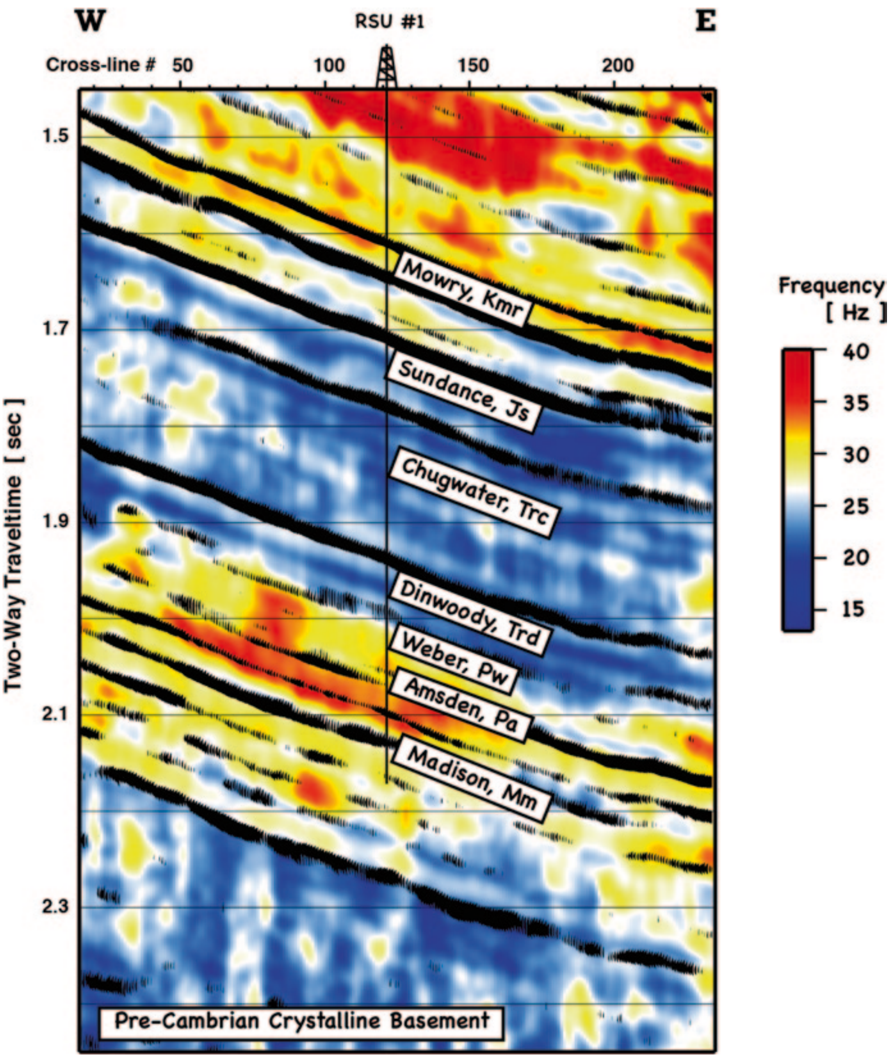

**Fig. 7.4** Interpreted west–east profile through the mean frequency volume at the RSU #1 well location. Seismic frequency image is co-rendered with seismic amplitude section (negative excursions are shown in black)

## 7.5.2 VSP Data Processing

The Baker Hughes processing team processed the seismic data acquired in the well through the following steps.

**Editing and Stacking** The three-component data was format-converted and referenced to the elevation of the source. The down-hole geophone traces for each depth level were edited as necessary and then stacked using a median summation technique. The stacked record was arranged according to increasing depth, and the first arrival times were picked. A time/depth curve was computed from the first break times. The accuracy of the depth sensor was checked by comparing the first arrival times during the *down* and *up* runs of the tool.

**Velocity Computations** The observed first arrival times at all depth levels were converted to vertical times, and then referenced to the Seismic Reference Datum (SRD = 7,500 ft above MSL), using a correction velocity of 9,000 ft/sc. These time-depth pairs were then used as input data for final velocity computations, which gave *average, RMS*, and *interval* velocities. [Tabulated and displayed in Electronic Supplementary Material, ESM Plate1]

**Acoustic Log Calibration** The VSP-derived velocity function was calibrated with the acoustic log over the 1,780 ft–12,717-ft measured depth interval below KB. (At each depth level the time difference (drift) between the VSP times and the acoustic times are computed. The drift time is added to all acoustic log values over the calibration interval. This effectively shifts the acoustic log to match the VSP-generated velocity values.)

**Synthetic Seismogram** An acoustic impedance log was computed by multiplying the calibrated acoustic log by the density log. A reflectivity series, showing primaries only (without transmission-loss effects), was derived from the acoustic impedance log. The reflectivity series was then convolved with a seismic wavelet to produce a synthetic seismogram. [The synthetic seismograms, having different frequency content and polarity, are shown in ESM Plate 2]

**Wavefield Separation** VSP wavefields consist of a superposition of the downward and upward traveling (or simply downgoing and upgoing) wavetrains. Both the downgoing and upgoing wavetrains are useful, but need to be separated before they can be studied and utilized. In this study, the wavefields were separated using a median filter. [The downgoing and residual upgoing wavefields are shown, respectively, in panels 2 and 4 of ESM Plate 3] The unwanted wave modes left in the dataset after the wavefield separation were removed by applying a seven-point median filter and zero-phase 10–80-Hz bandpass filter. [The upgoing wavefield at two-way time and the enhanced upwaves are displayed, respectively, in panels 5 and 6 of ESM Plate 3]

**Downwave Deconvolution** The VSP downwave deconvolution shapes the input source wavelet to zero phase and collapses upcoming multiple reflections generated above the depth of the deepest receiver. A 400-ms trace-by-trace deconvolution operator was computed and then applied to the downgoing and upgoing wavefields followed by a zero phase 10–80-Hz bandpass filter. [The deconvolved downgoing and upgoing wavefields are shown respectively in panels 3 and 7 of ESM Plate 3.]

**Corridor Window and Corridor Stack** The basic computed product of the VSP is known as a *corridor stack*, which in appearance resembles a synthetic seismogram. In reality it is a vastly superior well correlation tool, because it contains actual seismic reflections comparable with the surface seismic data. In this study, a narrow time window was designed to include only primary events with similar reflection character on enhanced deconvolved upwaves. The data that lies outside the stacking corridor was muted [panel 9 of ESM Plate 3]. The resultant muted traces were then stacked to one trace, called a *VSP corridor stack trace*. This stacked trace is repeated eight times for visual clarity and represents the seismic response at the RSU #1 wellbore. [The 10–80-Hz filtered corridor stack, with normal and reverse polarity, is shown, respectively, in panels 10 and 11 of ESM Plate 3]

**L-Plot Correlation Display** An L-Plot correlation display ties together the depth domain and time domain properties of the VSP with well-log data and synthetic seismograms. The VSP deconvolved upwaves are displayed with linear depth-of-trace spacing. Well-log data displayed in the depth domain are plotted above the upwaves panel using the same depth scale. In this way, the reflection events can be directly correlated in the depth domain with the well-log data [ESM Plate 4]. In addition to the depth-domain data, time-domain synthetic seismograms and well logs converted to time domain are also displayed using the same time scale as that of the deconvolved upwaves. This allows time domain event correlation between the well-generated data and VSP data [ESM Plate 4].

**Interpolated Time-Depth Table** The most basic information that we want from the VSP is a seismic time-to-depth relationship. This information was acquired by just picking the first-breaking energy of the direct arrivals. [The time-interpolated results (with 2-ms sample rate) are presented in tabular form in ESM Plate 5 for the two depth-reference points—the seismic reference datum and the kelly bushing of the RSU #1 well.]

## 7.6 Comparison of VSP and Surface Seismic (CMP) Data

The deconvolved and enhanced upgoing events show that the VSP wavefield separation and processing has been fairly successful. The seismic reflections corresponding to the major stratigraphic intervals are continuous across all traces (panel 8, ESM Plate 3). One can easily determine the time of the geologic interface that created the upgoing event by following the characteristic feature of this event up to its intersection with the time axis.

One of the main reasons for acquiring VSP data is to improve the analysis of CMP reflection data. In order to accomplish this objective there should be reasonable correlation between the two data sets. Figure 7.5 illustrates the surface P-wave reflection seismic data with the VSP inserted at the tie point (RSU #1 well location). The overall reflectivity trends of the surface reflection data and VSP data match well. The reflectivity is moderate within the interlayered sand and shale Cretaceous and Jurassic strata and very low within the shale-rich strata of the underlying Triassic formations (Fig. 7.5). The top and base of the major sealing horizon is obvious on the CMP data and the VSP; the relative amplitudes are also comparable

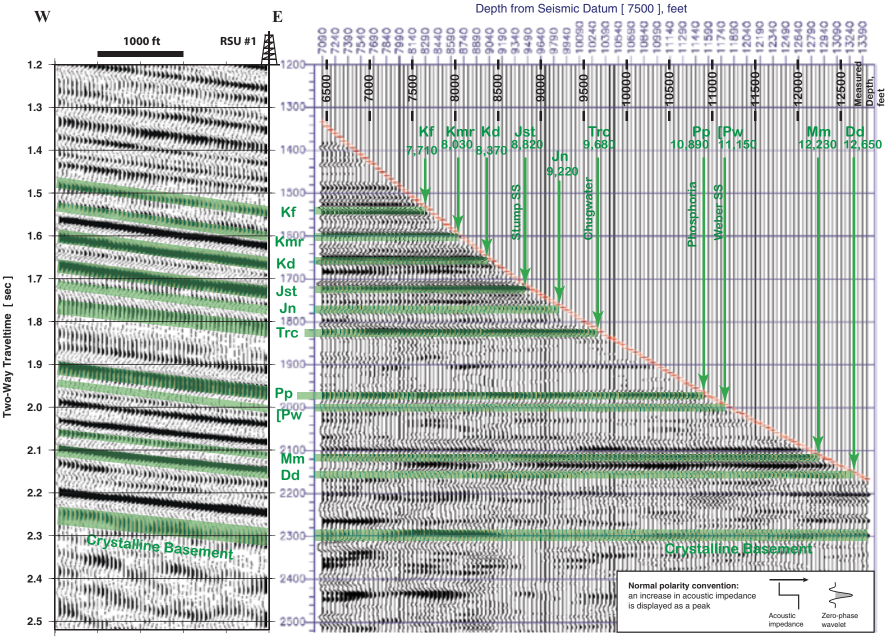

**Fig. 7.5** (**a**) Interpreted west–east profile (*left* panel) through the PSTM seismic volume with the RSU #1 well located on the east side. (**b**) upgoing (reflected) VSP wavefield displayed at the same time (*vertical*) scale as the surface seismic. *Green* highlights the interpreted seismic reflections

(1.83–1.97 s time interval in the VSP panel on Fig. 7.5). Going down in time, the reflectivity increases considerably within the carbonate-rich units of the Paleozoic Phosphoria, Weber, and Madison formations. At the RSU #1 well location, the top of the Weber Sandstone corresponds to a seismic trough at 2.0-s two-way traveltime (TWTT). The Madison Limestone is imaged with a reflection just below 2.1-s TWTT (Fig. 7.5). The seismic trough at a TWTT of 2.13 s at the well location corresponds to the low-impedance middle Madison unit.

The higher frequency content of the VSP data is evident. The prestack VSP traces (VSP panel on Fig. 7.5) show a series of distinct reflections just above and below the Triassic shales, whereas the same reflections on CMP data are overlapping and complex. This difference in frequency content allows for laterally continuous features to be better resolved in CMP data than in VSP data.

## 7.7 Comparison of VSP and Well Data (Geologic Property Modeling)

Forward modeling was used to gain insights into the geometrical and physical relationships between seismic reflection amplitude and rock/reservoir properties derived from the well logs and core. The modeling was limited to the one-dimensional case along the test well-bore axis within a depth interval that includes the major deep saline aquifers (10,500–12,700 ft below KB). The density and velocity values used in the modeling are based loosely on physical properties of the major target reservoir rocks (the Weber and Madison Formations) and confining units. The perturbed geologic models were convolved with seismic wavelet (10–80-Hz band pass) to produce simple, zero-offset acoustic models of the expected seismic response. These acoustic responses were further compared with the VSP stacked trace using a basic cross-correlation technique. Pearson's cross correlation coefficient was used as a criterion to validate the match between the modeled and observed data. The modeling iteration was stopped after obtaining a fairly strong $(r = 0.86)$ correlation coefficient between the synthetic response and VSP trace. For comparison, the starting model values (original velocity/density logs) produce a synthetic trace that correlates moderately with the observed VSP trace $(r = 0.69)$. The resultant geologic property model contains estimates of reservoir thickness, porosity, and permeability. [The tabulated property model and the corresponding synthetic trace, as well as the wireline log data and the VSP trace, are displayed in ESM Plate 6]

## 7.8 Horizon Mapping and Depth Conversion

This section reports results of using 3-D seismic (P-wave) data and RSU #1 well control to map Lower Cretaceous and pre-Cretaceous formations in the study area. The primary storage candidates on the Rock Springs Uplift are deep saline aquifers in the Pennsylvanian Weber and Mississippian Madison Formations. Hence, we focus on these formations as well as the overlying shaly horizons in the Triassic Chugwater and Dinwoody Formations and Cretaceous Mowry Shale (Fig. 7.6). In general, deep saline aquifers are excellent potential $CO_2$ storage candidates, but significant pre-storage characterization is required to determine their suitability.

Due to low seismic vertical resolution (~ 150 ft at target depth), reservoir and seal properties away from the well were characterized largely along seismic horizons rather than vertically. Any kind of seismic vertical profile interpretation will inevitably face the upscaling problem of fine-scale lithologies. This means that, for example, the velocity anomaly associated with high-porosity, thin sandstone bed will be smoothed (upscaled) and reduced through velocity averaging with the surrounding lithologies. On the contrary, horizon-based attribute variations are less dependent on lithologic change and can be more readily related to variations in physical rock properties and fluid content.

Figure 7.7 shows our deep structure mapping workflow. Structure mapping is a process of tracking identical wavelet features that correspond to a specific geologic formation (bedding plane) throughout the seismic volume. Formation tops were first tied to the 3-D seismic volume on the basis of our calibration of seismic data with VSP observations (Fig. 7.5). We then created synthetic seismograms of various polarity and bandpass combinations using sonic and density logs from the RSU #1 well. The results of the VSP-seismic calibration were further verified with these synthetic seismograms; this assured the fidelity of the seismic horizon interpretation completed for the well.

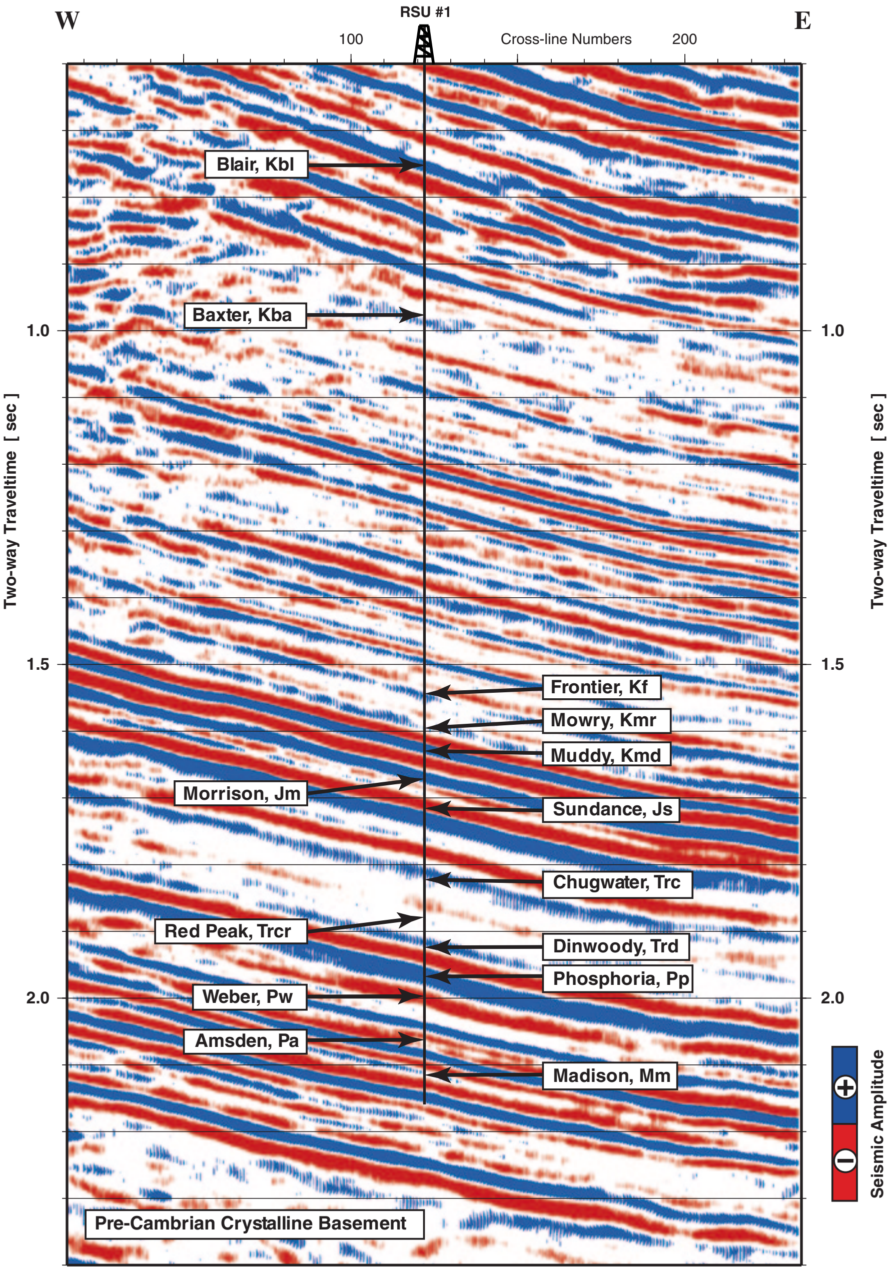

**Fig. 7.6** West–east vertical section through the seismic amplitude volume at the RSU #1 well location. Geologic interpretation (formation tops with symbols) was based on integrated analysis of the logs, VSP, and surface seismic data

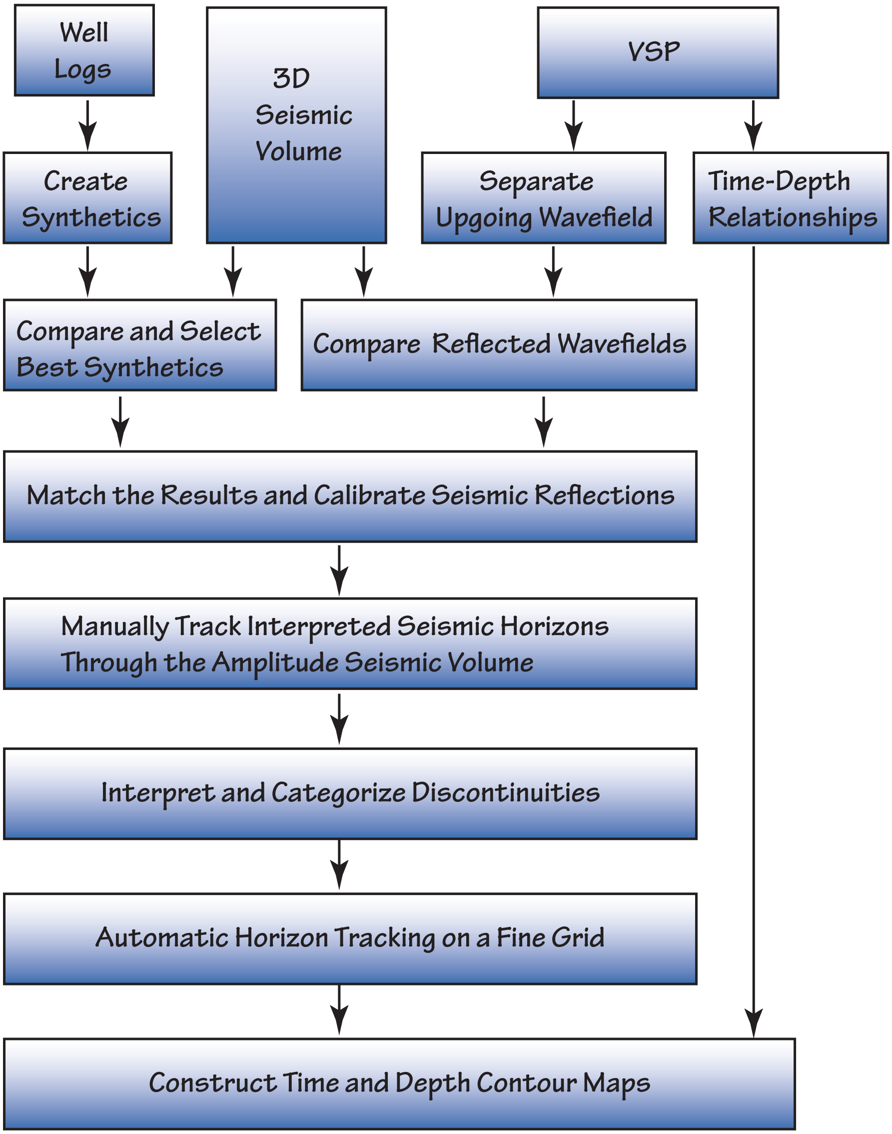

**Fig. 7.7** Block-diagram for structural mapping workflow

Depth structure maps were generated using the time-depth conversion table derived from VSP observations at the RSU #1 well. To achieve uniform depth gridding, the results of the transformation were interpolated using a cubic spline algorithm. To match with well observations, the depth-transformed horizon picks were corrected to the KB datum.

Most interpreted horizons appear to be laterally continuous throughout most of the survey area, but this continuity ceases in the Jim Bridger Power Plant area in the northeast and the I-80 interstate in the southwest parts of the area (Fig. 7.1). Acquisition footprints due to irregular coverage compromise the seismic images beneath these areas: any subsurface mapping and interpretation of discontinuities in these areas is doubtful with respect to possible $CO_2$ migration pathways. Both time structure and depth structure maps of the Frontier through Madison Formations (youngest to oldest in Fig. 7.6) were produced and interpreted. For reservoir characterization purposes, it is useful to extract seismic attributes not coincident with the tracked horizon but conformal to it and shifted by a chosen number of milliseconds. These horizons, usually called the *phantom horizons*, were also used in this study.

## 7.9 Seismic Attributes

In this study, seismic attributes are recognized as measures of seismic data that lead to better understanding of the subsurface and thus reduce uncertainty in geologic interpretations. Seismic attribute analysis can play a significant role in reservoir property prediction by revealing information that may not be evident in the standard amplitude data. A suite of properties of a seismic trace (such as amplitude, phase, and frequency) can be crossploted with the corresponding well logs to show the relation between the two types of data. The attributes selected on the basis of close correlation with petrophysical properties can be effective in estimating reservoir properties away from the well.

Seismic attributes can be divided into two broad categories, those that help quantify the *geometrical* component of seismic data and those that help quantify the *physical* component of seismic data. The geometrical (morphological) attributes help extract information on reflector dip, azimuth, and terminations, which can be related to faults, karst, and fractures. The physical attributes (seismic event magnitude, frequency and waveform characteristics, propagation velocity) can be related to lithology, porosity, reservoir thickness, or pore-fluid content.

In this study, both stacked amplitude volume and prestack CMP gathers were used to perform the basic seismic measurements necessary to derive attributes. The basic parameters that were measured are travel-time, amplitude, waveform, and frequency. From this information it was possible to compute:

- Velocity—from measurements of delay times and amplitudes along seismic reflections
- Time and depth maps of important horizons—from travel-times (and velocity information)
- Contrast in physical rock properties (velocity and density)—from measurements of reflection amplitude
- Locations of faults and intense fracturing—from discontinuities in seismic reflectivity patterns
- Dip magnitude and azimuth of beddings—from travel-time differences along a reflecting surface
- Stratigraphic changes—from instantaneous frequency measurements

The goal of this seismic attribute computation was to provide quantitative information interpretable in terms of porosity and permeability necessary for fluid flow simulation within these target reservoirs. Locating impermeable barriers to flow as well as assessing the integrity of confining layers was also within the scope of our research. The attempt was made to not overwhelm the study by calculating seismic attributes that lack geologic significance or have no clear physical meaning. Thus, our foremost criterion for selecting attributes was a physical basis for correlation between properties measured in the well bore and the core. For example, interval velocity has a physical correlation with porosity: as velocity increases, porosity typically decreases. Therefore, the scope of this study comprised only the few attributes discussed below.

### *7.9.1 Definition and Computation of Basic Attributes Used in This Study*

**Reflection Strength** Reflection strength is one of the basic outputs of the complex seismic-trace analysis first described by Tanner et al. (1979). The complex trace $C(t)$ is defined as:

$$C(t) = S(t) + \mathrm{i}Q(t), \tag{7.1}$$

where $S(t)$ is the seismic trace, $i = \sqrt{-1}$ , and $Q(t)$ is the quadrature of the seismic trace (Hilbert-transformed component of $S(t)$, or 90° phase shifted $S(t)$).

The reflection strength is the modulus of the complex function:

$$R(t) = \sqrt{S^2(t) + Q^2(t)}, \tag{7.2}$$

where $R(t)$ represents the envelope of the seismic trace signal that is related directly to the acoustic impedance contrast. It may depict an individual interface contrast or, more likely, the combined response of several interfaces. Reflection strength is a physical attribute that can be used to discriminate major changes in lithology and deposition environment, sequence boundaries, pore-fluid content, unconformities, and lateral changes due to porosity variations and faulting.

**RMS Amplitude** RMS amplitude is another measure of seismic trace reflectivity that is measured within a time window. Specifically, it is the square root of the sum of the squares of the amplitudes within the window interval and is independent of amplitude sign. It is conventionally used as a direct hydrocarbon indicator in the search for “bright spots” or “dim spots.” The attribute indicates anomalous amplitude zones and may serve as a lithology and porosity indicator. In this study, we used a 50-ms window for the RMS amplitude calculation, which is equivalent to a 20-Hz signal.

**Mean Frequency** The mean frequency, actually the weighted mean frequency, is derived from a spectrally decomposed seismic trace (generated through a Fourier Transform in this study). The weighted mean is similar to the arithmetic mean, and is used in situations where instead of each sample frequency contributing equally to the final average, some frequencies contribute more than others. The degree of contribution (weight) is defined by the spectral amplitude value. In the digital signal processing literature the weighted mean frequency is often termed the spectral centroid frequency (or simply the centroid frequency) because it indicates the location of the "center of mass" of the spectrum. Formally, the weighted mean frequency $F$ of a set of frequencies $\{f_1, f_2, \dots, f_n\}$ with weights $\{a_1, a_2, \dots, a_n\}$ is the quantity:

$$F = \frac{\sum_1^n a_i f_i}{\sum_1^n a_i}. \tag{7.3}$$

**Bandwidth Attribute** The bandwidth attribute is estimated as the variance with respect to the centroid frequency (standard deviation) that indicates the width of the amplitude spectral distribution $\{a_1, a_2, \dots, a_n\}$ over a band of frequencies $\{f_1, f_2, \dots, f_n\}$. Both the bandwidth and the mean frequency are statistical measures of seismic wavelets and relate to various physical conditions of energy transmission, such as bed thickness variation, change in seismic facies, relative absorption characteristics, and variable pore fluid content. The final seismic frequency content is a comprehensive result of many factors prominent among which are the source wavelet, the lithologic properties of the strata, and the application of seismic data processing.

**Spectral Decomposition** The spectral decomposition algorithm, used in this study for several attribute computations, is based on a Short Time Fourier Transform (STFT). The general Fourier Transform relates a waveform (a function of time) to its spectrum (a function of frequency). If the time band of the waveform is multiplied by a constant, then the bandwidth of the spectrum is divided by the same constant. This property is an expression of the Heisenberg uncertainty principle with respect to seismic processing. Simply speaking, if one wants to gain better resolution in time, he must pay for it with resolution reduction in the frequency domain. The spectral decomposition software used in this study implements STFT by choosing frequency-domain windows as opposed to time-domain windows. STFT can be seen as the filtering of a signal through a set of fixed bandwidth band-pass filters whose center frequencies are distributed uniformly along the frequency axis. To bypass the Heisenberg uncertainty principle, we implemented a sort of multiresolution STFT by combining (or averaging) individual spectrograms with different time-frequency resolutions. The *spectral amplitude attribute* that is often referred to in this study is the iso-frequency magnitude resulting from spectral decomposition. This attribute is always computed normalized to the maximum magnitude value.

**Velocity Attribute** The velocity attribute was derived from stacking-velocity analysis applied to prestack CMP gathers. High-density, high-resolution interval velocity volume was calculated using an automated routine that performed velocity analysis at every time sample and at every CMP location. For the homogeneous earth with planar interface, the travel-time curve of the reflections for various offsets between source and receiver is conventionally calculated using:

$$t^2 = t_0^2 + \frac{x^2}{v_{stack}^2}. \tag{7.4}$$

At every CMP gather (with source-receiver offsets $x$) and every time sample $t_0$, a velocity spectrum is calculated for a set of trial stacking velocities $v_{stack}$ using semblance as a coherency measure. The semblance value reflects how well the model path corresponding to the trial velocity $v_{stack}$ fits the actual trajectory of reflected signals in the data. The semblance $S$, as defined by Neidell and Taner (1971), is given by the equation:

$$S = \frac{\sum\left[\sum a(t,x)\right]^2}{N\sum\sum a(t,x)^2} \tag{7.5}$$

The inner sums in this equation are over $N$ traces having various offsets $x$, while the outer sums correspond to time smoothing with the operator centered at time index $t$. Semblance is maximized when the values $a(t, x)$ do not vary with index $x$. Time smoothing is necessary to increase semblance stability for coherent events located close to zero-crossings. Within the computer code, the velocity spectrum is estimated with relatively few trial velocities (25 in this study) and is fitted to a Gaussian curve:

$$f(x) = b + pe^{(-0.5(x-c)/w)^2}, \tag{7.6}$$

where $b, p, c$, and $w$ represent the *base* (semblance shift), *peak* (peak semblance value), *central point* (central or mean velocity value), and *width* (velocity standard deviation) of the Gaussian distribution, respectively. A velocity distribution fitted with the Gaussian formula enables precise and unambiguous estimation of the peak semblance value and the corresponding stacking velocity. When computation over the trace samples ($t_{0i}$) is complete, the resultant stacking velocity function is smoothed with an operator whose size is proportional to the time $t_0$ and velocity standard deviation (parameter $w$ in the Gaussian curve equation) at that time. The smoothed stacking velocity function is further processed using Dix's formula (1955) to produce interval velocities that can be readily interpreted in terms of lithology, pore-fluid or porosity variations.

**Acoustic Impedance (AI)** Acoustic impedance (the product of the rock density and velocity) is a basic physical property of rocks that is commonly calculated from corresponding density and sonic well logs. AI has the benefit over seismic reflectivity data in that it is a layer property that can be directly related to lithology and to changes due to fluid production/injection. A problem arises when the well-log data is not adequate to image the targeted subsurface. Additionally, reservoir heterogeneity may require more control than from existing well locations alone: in this case (including our study), an acoustic impedance volume can be created through inversion of the P-wave seismic volume.

Our inversion scheme followed an approach known as *synthetic sonic log* section (volume) generation, described first by Lindseth (1979). In outline, the inversion operations included (1) computation of an approximate reflection coefficient sequence using post-stack seismic amplitude volume, (2) inversion of the reflection coefficients to band-limited, high-frequency velocity coefficients, and (3) use of (2) to modulate low-frequency velocity components, obtained from high-density reflection velocity analysis, to produce synthetic sonic logs. If the subsurface density distribution is known (or estimated), it can be incorporated in this scheme to produce synthetic acoustic impedance logs. In our study, we verified the accuracy of the inverted synthetic volumes by comparing them with the corresponding logs from the RSU #1 well. The P-wave *synthetic sonic log attribute* obtained in this study combines the features of stacked amplitude and interval velocity volumes. Namely, it derives its volumetric property (rather than an interface property) from the interval velocity field, and it derives better resolution from the amplitude volume. Inverted data, a layer property, is a more intuitive tool that allows one to tie lithology and fluid presence to seismic data.

**Seismic Coherency** Seismic coherency is a measure of the consistency of seismic reflections. In other words, it quantifies the similarity in appearance and shape of seismic waveforms from trace to trace. Where events are similar, coherency is high. Low-coherent, discontinuous reflections may be caused by variation in structure, stratigraphy, lithology, porosity, and pore fluids. The semblance-based coherence attribute estimation in this study was performed on post-stack amplitude data. The basic algorithm of coherency estimation can be summarized as follows: for each point in a 3-D seismic volume, compare the waveform of adjacent traces over a short vertical window. At the same time, uniformly tilted strata should not affect the coherency computation.

This was accomplished in the following steps. First, for each volume sample, a small reflection surface (3×3 horizontal samples) is identified around the central sample. The surface coordinates at trace intersections are calculated by finding the maximum cross-correlation value over a vertical analysis window between the central trace and each surrounding trace. A parabolic fitting technique is used for precise time shift (tilt) identification that corresponds to the maximum value of the cross-correlation between the discrete trace samples. The inter-trace tilt effect is removed and the semblance value is calculated using Eq. 7.5 for the spline-interpolated trace samples. For the coherence attribute calculation, the inner sums in the semblance equation (Eq. 7.5) are over $N$ tilt-corrected traces $x$, while the outer sums correspond to time smoothing with the operator centered at time index $t$. As with semblance-based velocity analysis, time smoothing is necessary to increase semblance stability for coherent events located close to zero-crossings.

**Curvature Attribute** In a general sense the seismic curvature attribute is a measure of how deformed a reflecting surface is at a particular location. The more deformed the surface, the larger its curvature. With respect to geometry, curvature is defined as the reciprocal of the radius of curvature, and correspondingly, belongs to the geometrical category of attributes. The suite of curvature attributes utilized in this study, comprises dip magnitude, dip azimuth, maximum and minimum, and strike and dip curvatures. Analysis of these attributes can help remove the effects of regional dip and emphasizes small-scale features such as tight folds, faults, karst, and fractures.

The estimation of volumetric curvature attributes is performed in three stages. First, for each volume sample, a small reflection surface (3 x 3 horizontal samples) is identified around the central sample. The surface Z-positions are calculated by finding the maximum cross-correlation value over a vertical analysis window between the central trace and each surrounding trace. A parabolic fitting technique is used for precise time shift (tilt) identification that corresponds to the maximum value of the cross-correlation between the discrete trace samples. Next, a least-squares quadratic surface Z (X, Y) is fitted to the data within the analysis range. Finally, the set of curvature attributes is computed from the coefficients of the quadratic surface using traditional differential geometry (Roberts 2001). At any point of the surface, the curvature (positive or negative) can be measured at any azimuth. One of these azimuths will yield the largest curvature. This curvature is named the *maximum curvature* and the curvature at the orthogonal azimuth is named the *minimum curvature*. The *maximum* and *minimum curvature* attributes are very effective at delimiting faults and fault geometries, with maximum curvature corresponding to the up-thrown (positive) side of a fault. The curvature attribute extracted in the direction of maximum dip is named the *dip curvature*, while the one extracted in the orthogonal direction (along strike) gives us the *strike curvature*. The last two attributes can be especially useful in examining the local surface morphology and interconnectivity that can help explain buoyancy-driven processes and fluid migration pathways. The curvature attributes described above are lateral second-order derivatives of structural relief components of the seismic time- (or depth)-of-reflection events. This is what makes them so sensitive to subtle structural variations. In contrast, the *dip magnitude* and *dip azimuth* are derived using first-order derivatives, which allows using them as regional structural trend indicators.

## 7.10 Seismic Interpretation

The 3-D seismic data and vertical seismic profiling (VSP) constituted information essential for delineation of structural trends and stratigraphic correlation. Of the available geophysical logs from the RSU #1 well, the $\gamma$-ray, photoelectric factor, resistivity, and neutron porosity logs were primarily useful for general rock/fluid identification and petrophysical analysis. The sonic and density logs were used for porosity and permeability estimation.

### *7.10.1 Method of Interpretation*

A collection of seismic attributes, as described in Sect. 7.9.1, was used for predicting the distribution of physical properties (e.g., porosity, fracture density) of the strata being imaged seismically. It must be understood, though, that most of the links between reservoir properties and seismic attributes are not well established, and that these correlation results may thus be tenuous, questionable, or difficult to explain. Even today, there is a lack of systematic effort by scientists to establish the physical

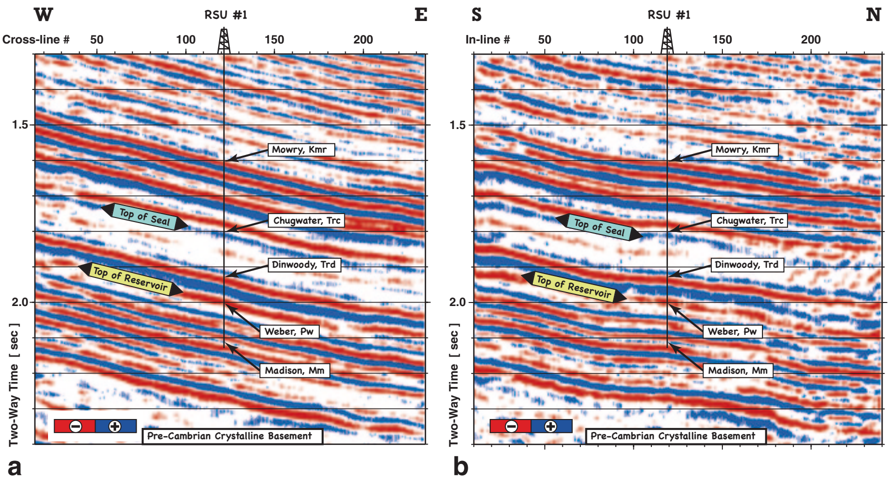

**Fig. 7.8** Interpreted (**a**) west–east and (**b**) south-north vertical sections through the seismic amplitude volume at the RSU #1 well location. Note northeast-dipping reflections on both sections

basis for such relationships, and this is especially true for the Rocky Mountain region. The method used in this study is more qualitative than quantitative. No attempt was made at rigorous numerical modeling; rather, the effort focused on identifying of geobodies (or seismic facies) that share similar attribute properties or a similar set of attribute properties within a seismically imaged volume. These geobodies were calibrated (or tested) with geologic studies and log-derived physical properties.

Attributes-based interpretation takes advantage of the wealth of seismic information available and offers a more efficient way of representing data than conventional methods. Attribute interpretation supplements conventional structural interpretation because the discriminating properties of the attributes may be critically checked for their relevance for a particular structural feature. Therefore, most of the figures presented in this study were produced using blended techniques: for the 2-D vertical sections, derived color-coded attributes are combined (co-rendered) with seismic reflected-amplitude data; and for the map (plan) views, color-coded attribute values are combined with horizon contours. Below, we use vertical sections as the first step toward 3-D interpretation, followed by horizon slices (Sect. 7.10.3).

### *7.10.2 Interpretation—the Use of Vertical Sections*

The study site lies on the east flank of the Rock Springs Uplift, and correspondingly, seismic reflections image the area as a northeast-dipping monocline (Figs. 7.3 and 7.8). Assuming our estimated average P-wave velocity of the target formations to be 18,000 ft/s, the dip ranges from 2 to 8° within the imaged subsurface. The overall strong reflectivity of the subsurface is caused by significant variations in physical rock properties of sediments overlying the crystalline basement (Fig. 7.8). The RSU #1 well was used to identify the main horizons in the interpretation. With an accuracy of about 20 ms, we were able to track through the seismic time volume the tops of the following units, from top to bottom: the Frontier Formation (*Kf*), Mowry Shale (Kmr), Muddy Sandstone (*Kmd*), Morrison Formation (*Jm*), Sundance Formation (*Js*), Chugwater Formation (*Trc*), Red Peak Member (*Trc*), Dinwoody Formation (*Trd*), Phosphoria Formation (*Pp*), Weber Sandstone (*Pw*), Amsden Formation (*Pa*), and Madison Limestone (*Mm*).

The west-east vertical section with the interpreted formation tops is presented in Fig. 7.6. As is indicated in Fig. 7.8, the top of the major sealing interval coincides with the top of the Chugwater Formation. In the study area, the Chugwater Formation (labeled "Top of Seal" in Fig. 7.8) is composed mostly of seismically transparent, massive rock layers marked by low reflectivity. The seismic reflections intensify as they approach the "Top of Reservoir" interval corresponding to the Weber Sandstone (Fig. 7.8). It is the strong velocity/density contrast between the low-porosity reservoir rocks and the confining layers that increases the intensity of the corresponding reflections.

The RMS amplitude attribute provides better insight into lithologic variations within the strata drilled by the RSU #1 well. Zones of intense reflectivity in Fig. 7.9 are color-coded red and correspond to the following lithologies, from top to the bottom: the Rock Springs coal beds, Mowry Shale and Dakota sandstones, and carbonate rocks interlayered with shales. Blue intervals in Fig. 7.9 correlate with the massive (more uniform and homogeneous) shales, mudstones, and crystalline basement rocks that are almost transparent to the passing seismic energy. For the purposes of our project, it is important to note that an extensive blanket of thick and uniform Chugwater shales overlies the target reservoir rocks (the Weber Sandstone and Madison Limestone).

Seismic interval velocity provides an important clue in lithology identification, porosity distribution, and discrimination of pore fluid properties in subsurface rock/fluid systems. Hence, much effort was put into pre-stack data conditioning for velocity analysis and parameter tuning for an automated velocity computation routine. The resultant interval velocity volume shows great velocity variability in both vertical and lateral slices. Importantly, these seismic velocity variations correlate with lithological units, and do tie with sonic and VSP measurements. Figure 7.10 shows an interpreted west-east profile through the interval velocity volume at the RSU #1 well location. The upper part of Fig. 7.10 (0.4 to ~1.7 s two-way traveltime) images the Cretaceous strata that is characterized by significant velocity fluctuations around the mean value of about 14,000 ft/s. The velocity begins a rapid increase at the base of the Cretaceous rocks and reaches values of 20,000–22,000 ft/s at the top of the Precambrian crystalline basement. The seismically derived vertical velocity distribution agrees well with the trend seen in sonic P-wave velocity (Fig. 7.10).

A pronounced decrease in interval velocity is clearly observed at the base of the Cretaceous-age rocks (blue interval below ~1.6 s two-way traveltime in Fig. 7.10). This reduction in seismic (and also sonic) interval velocity highlights an interval that extends from the top of the Frontier Formation down into the Morrison Formation. The ~1,000 ft of interlayered shales, siltstones, and sandstones shown in Fig. 7.11 contains multiple intervals in which velocity drops below 12,000 ft/s. We interpret this anomalous velocity zone to be related to the generation of hydrocarbons,

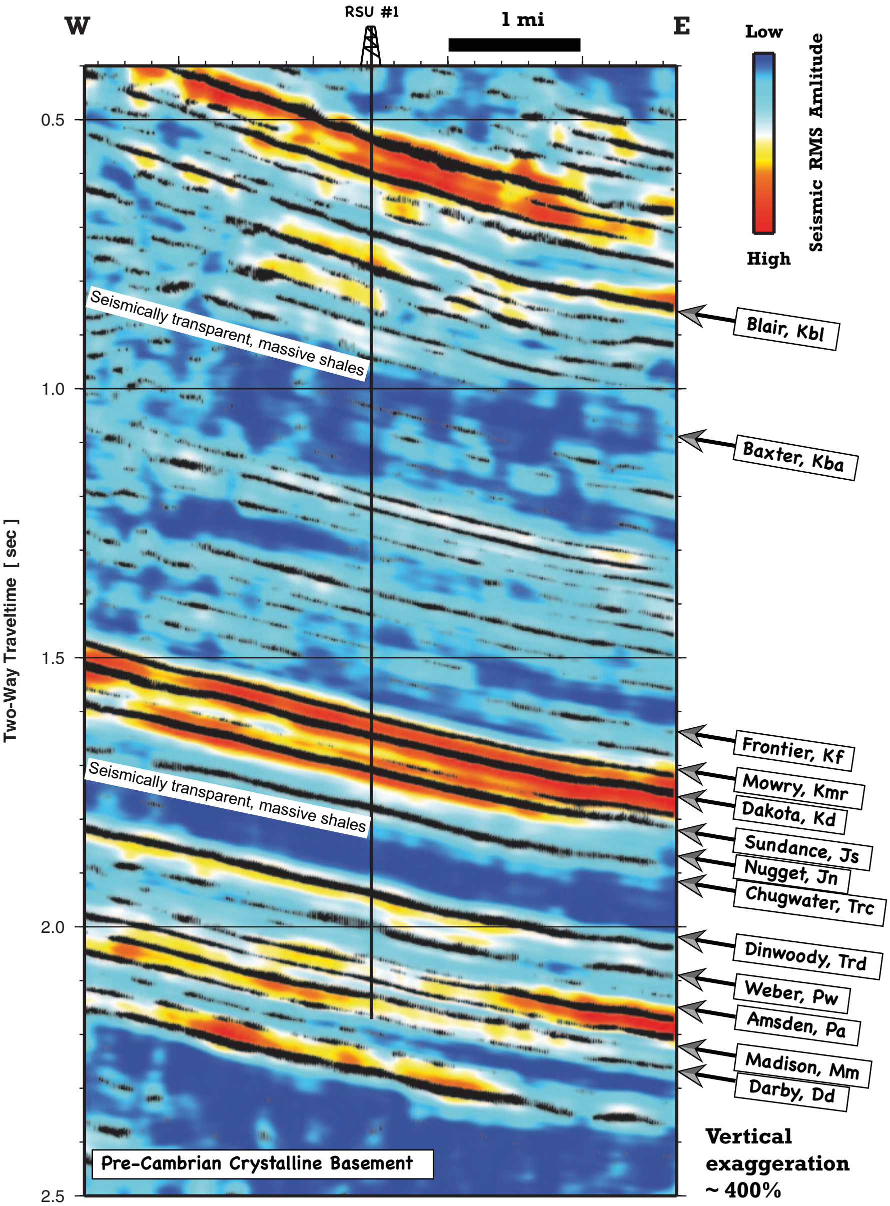

**Fig. 7.9** Interpreted west–east profile through the RMS amplitude volume at the RSU #1 well location. The color-coded RMS-amplitude image is co-rendered with conventional amplitude section (negative excursions are shown in black)

particularly gas, at the time of maximum depth of burial of the source rocks. The Rocky Mountain foreland basins, including the Greater Green River Basin, have undergone a complex geologic history starting with a principal subsidence phase,

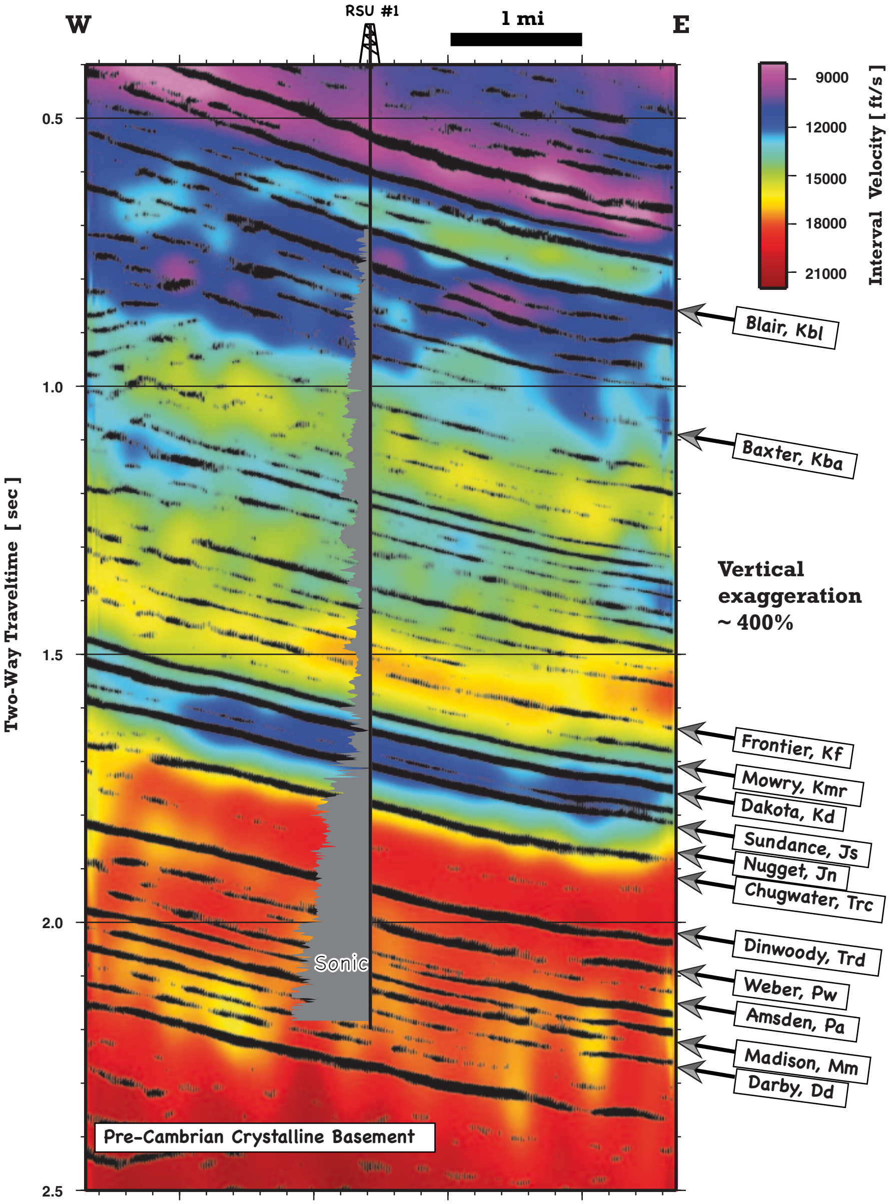

**Fig. 7.10** Interpreted west–east profile through the interval velocity volume at the RSU #1 well location. The color-coded velocity image is co-rendered with seismic amplitude sections. Time-transformed sonic log image (*gray*) is overlaid for velocity comparison

during which most of the basin-filling sediment was deposited, followed by one or more periods of uplift during which substantial amounts of sediment were eroded (Cluff and Cluff 2004). We speculate that gas was generated in the study area within

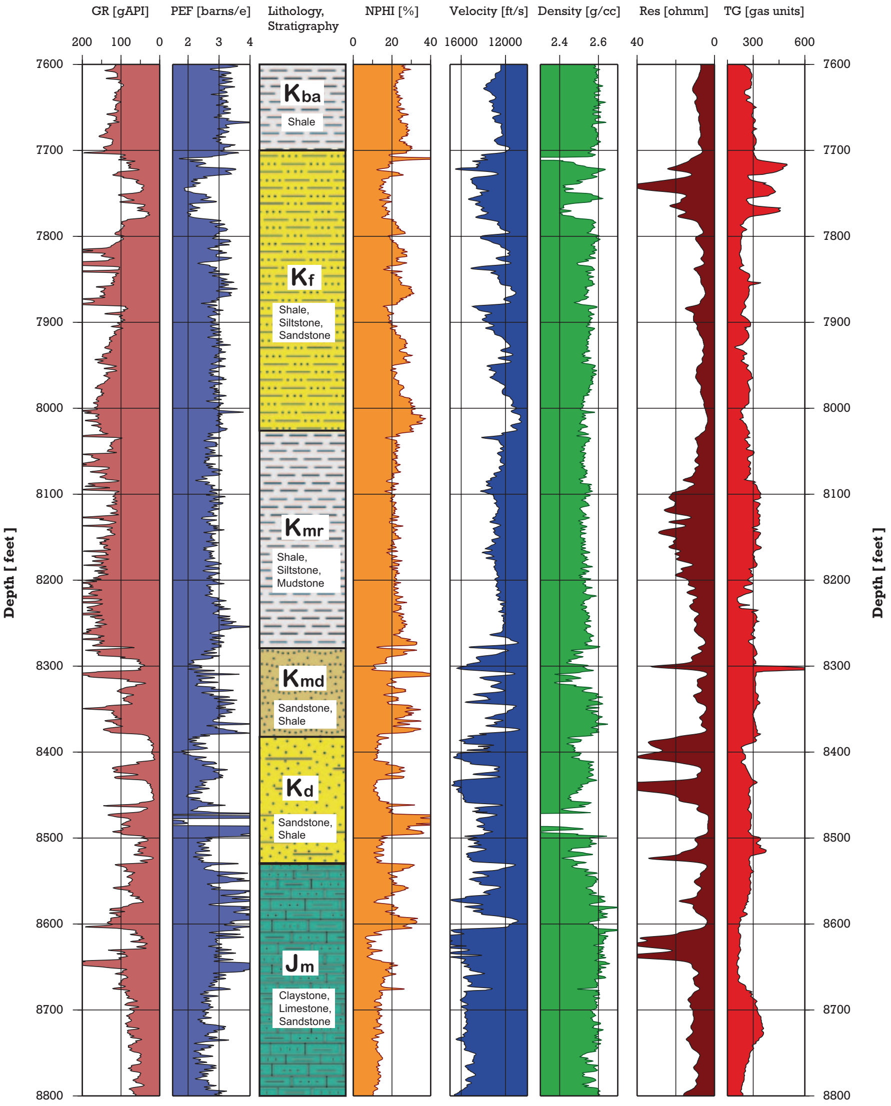

**Fig. 7.11** Interpreted wireline logs from the RSU #1 well over the depth interval with gas shows. From *left* to *right* the panels are: gamma-ray (*GR*), photoelectric factor (*PEF*), lithology and stratigraphy, neutron porosity (*NPHI*), P-wave velocity, deep resistivity (*Res*), and total gas (*TG*) from mud log

the Cretaceous shales at the time of their maximum burial. Constrained by the low permeability of fine-grained shales and siltstones, the gas could not migrate freely, which caused pressure to increase to the point where microfractures were induced, creating migration pathways. The process of gas generation, pressure increase, fracture opening, and migration continued until the gas had migrated into the more accessible units within the interval that extends from the Morrison Formation upward into the top of the Frontier Formation. The high pressures that were attained during gas generation at maximum burial likely decreased with uplift and erosion in the Late Cretaceous–Early Tertiary, leaving a record of modest present-day pressures that are far less than the paleo-overpressures. We think that sonic and resistivity logs through the Lower Cretaceous section (Fig. 7.11) retain a strong signature of reduced velocity and reduced resistivity directly related to microfractures opened during gas generation. Rock fabric affected by gas generation and associated microfracturing remained unchanged as the section was uplifted. Thus, the sonic and resistivity anomalies, unlike pressure conditions, are irreversible and reveal a signature of the former overpressure (Cluff and Cluff 2004). Geophysical well logs from the RSU #1 well support the proposed correlation between velocity/resistivity anomalies and aligned (parallel to bedding) microfractures in the Lower Cretaceous strata. Note that sonic velocity decreases as resistivity decreases (Fig. 7.11), which agrees with the velocity measurements in the direction perpendicular to bedding (sonic-log tool) and resistivity measurements in the horizontal direction parallel to bedding (induction-log tool). Although multiple gas-show records (total gas (TG) panel Fig. 7.11), no commercial gas inflow was reported while drilling the RSU #1 well. However, several wells in the seismic study area currently produce natural gas from the Frontier Formation.

Seismic inversion for acoustic impedance enhances the vertical resolution of the corresponding interval-velocity volume. This allows for more confident identification of beds having thickness comparable with the theoretical seismic resolution (one-quarter wavelength λ/4). A west-east vertical section through the acoustic impedance volume with the interpreted formation tops is shown in Fig. 7.12. Unlike the corresponding reflectivity section (Fig. 7.6), acoustic impedance is more readily related to lithology. For example, the Rock Springs coal beds are easily identifiable at early times by their extremely low values (Fig. 7.12). The Late Jurassic–Early Cretaceous source rocks that are responsible for gas generation are also characterized by low impedance values and show better discrimination. The Weber Sandstone and Madison Limestone also show noticeable contrast with the confining layers in Fig. 12. The acoustic impedance contrast for these units is due to enhanced porosity in these reservoir rocks. The impedance-porosity dependence is clearly observed on the crossplots presented in Fig. 7.13. Unlike the major reservoir rocks, the confining shale interval within the Chugwater and Dinwoody Formations is characterized by increased impedance values and a more homogeneous appearance (Fig. 7.12). This allows us to interpret these shales as low-porosity, thick, and laterally continuous.

Figure 7.14 shows three west-east coherence sections one mile apart. Geologicly, highly coherent seismic waveforms indicate laterally continuous lithology, while abrupt changes in waveforms can indicate faults and fractures in sediments. There are several sub-vertical, low-coherency zones that we interpret as potential faults (between red arrowheads in Fig. 7.14). The more prominent of these faults are within Upper Cretaceous strata (above 1.5 s in Fig. 7.14). The time interval with reflections from the target reservoir rocks appears to be laterally more continuous, with possible faulting down-dip of the RSU #1 well (northeast of the well—red arrows).

The basement-involved faulting northeast of the RSU #1 well is more obvious in the color-coded mean-frequency images (Fig. 7.15). The mean frequency of seis-

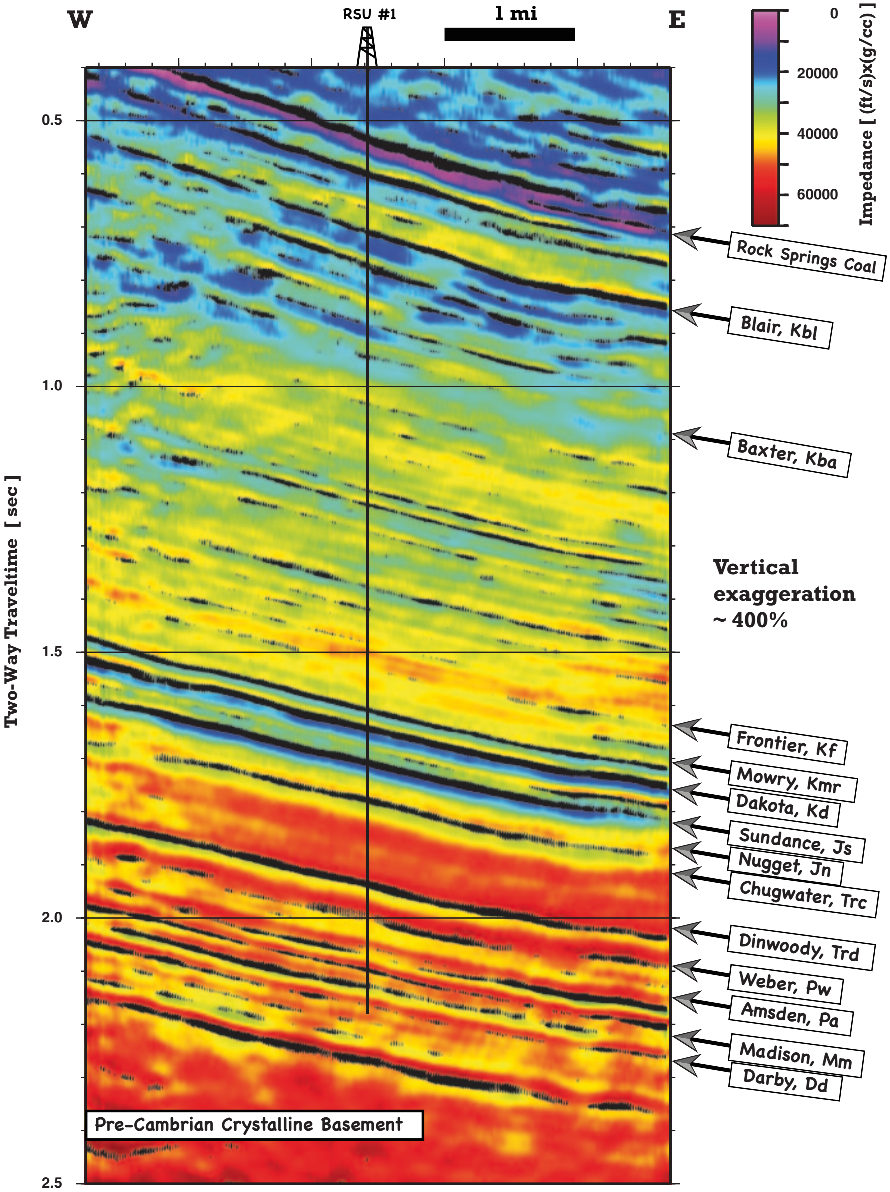

**Fig. 7.12** Interpreted west–east profile through the acoustic impedance volume at the RSU #1 well location. The color-coded impedance image is co-rendered with seismic amplitude section

mic wavelets is related to absorption characteristics in the subsurface, with higher frequencies more attenuated than lower frequencies over a fault zone. Hence, the steeply dipping, sub-parallel structures northeast of the well in Fig. 7.15 are interpreted as potential faults. Frequency can also be used to delineate geologic forma-

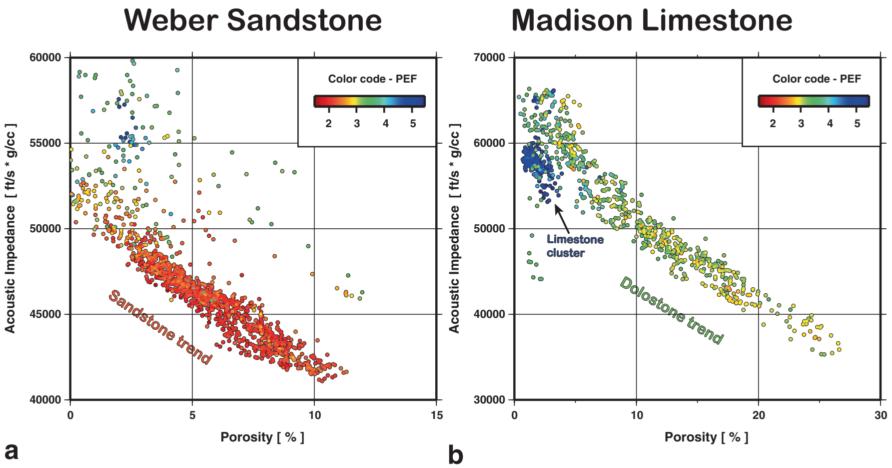

**Fig. 7.13** Acoustic impedance versus density porosity crossplots color-coded with the photoelectric factor (*PEF*). The measurements are from the RSU #1 well within the depth intervals: (**a**) 11,150–11,810 ft (Weber Sandstone), and (**b**) 12,230–12,650 ft (Madison Limestone). Note a pronounced inverse trend in both distributions, that is, acoustic impedance decrease with increasing porosity of the major reservoir rocks

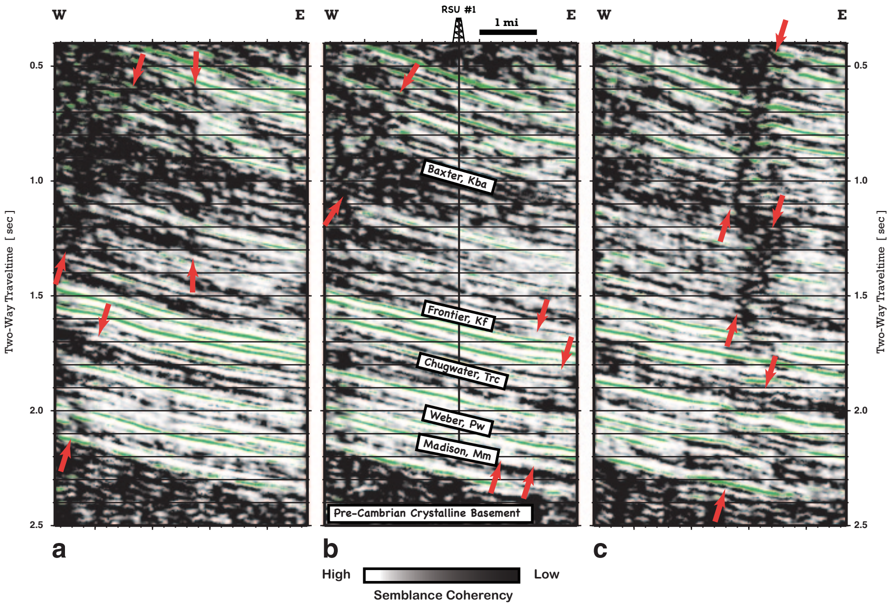

**Fig. 7.14** West–east profiles through the coherency volume: (**a**) one mile south of the RSU #1 well location, (**b**) at the RSU #1 well location, and (**c**) one mile north of the RSU #1 well location. The *gray*-scaled coherency image is co-rendered with seismic amplitude section (*green* reflectors). Low-coherency zones (dark color) with sub vertical orientation are interpreted as potential faults (*red arrowheads*)

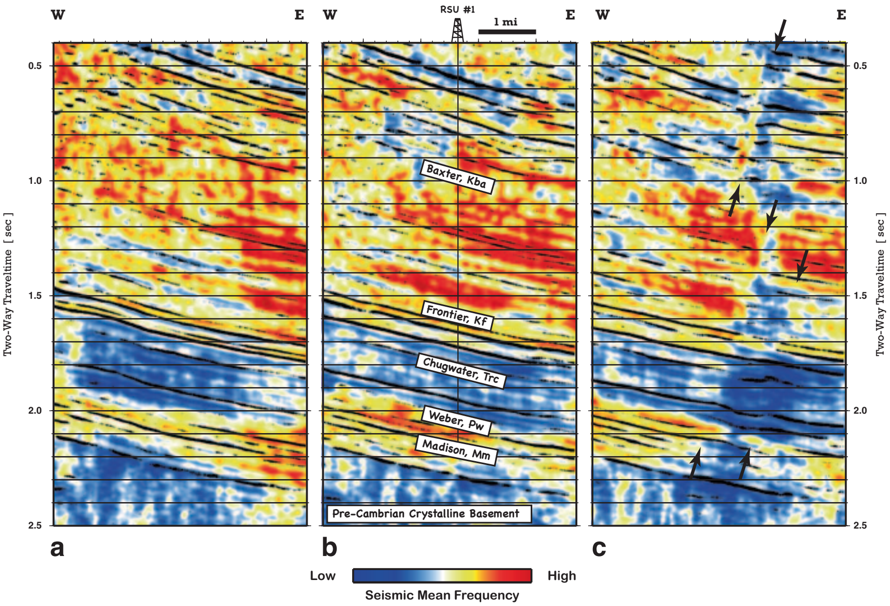

**Fig. 7.15** West–east profiles through the frequency volume: (**a**) one mile south of the RSU #1 test well location, (**b**) at the RSU #1 well location, and (**c**) one mile north of the RSU #1 well location. The color-coded frequency image is co-rendered with seismic amplitude section (*black* reflectors). The steeply dipping structures separated with low-frequency zones (*blue*) are interpreted as potential faults (*black arrowheads* in panel c)

tions, likely as a result of wave interference in different lithologies. The Chugwater Formation, a Triassic red bed, has a distinctly low mean seismic frequency with respect to the underlying targeted reservoirs (Weber and Madison Formations) and overlying Jurassic and Cretaceous units. The characteristic low seismic frequency of the Chugwater Formation was used to help define the lateral continuity of this sealing unit across the study site.

### *7.10.3 Interpretation—The Use of Horizon Slices*

The attribute anomalies discussed in Sect. 7.10.2 are most readily apparent when presented along the interpreted seismic horizons (Fig. 7.6) in the form of attribute *horizon slices*. Attributes examined in this section are the reflection strength, mean frequency, coherence, curvature, dip azimuth and magnitude, spectral amplitude, and synthetic sonic log attributes. Permeability modeling based on petrophysical and attribute analysis is discussed in Sect. 7.11. Here, we present only those figures that demonstrate well-developed trends in attributes or are related to targeted reservoir/seal characterization.

The *structural configuration* mapped from 3-D seismic data clearly depicts a northeast-dipping monocline at all stratigraphic levels examined (Figs. 7.3 and 7.16). The strata are almost flat in the northeastern part of the study area, but their

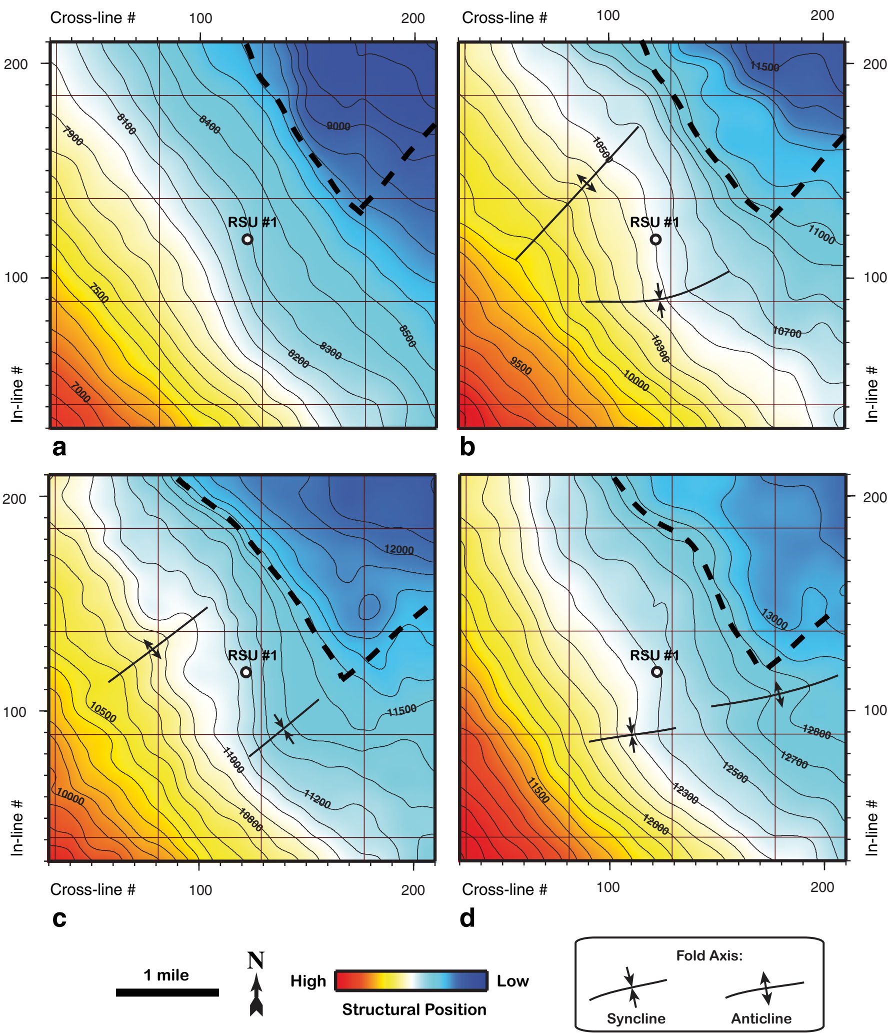

**Fig. 7.16** Color-coded structure maps of the interpreted seismic horizons: (**a**) Muddy, (**b**) Dinwoody, (**c**) Weber, and (**d**) Madison. Contour interval is 100 ft for all maps. The depth reference point is Kelly bushing (*KB*) at the RSU #1 well. *Dashed lines* show interpreted faults

dip steepens to about 8° in the southwest part (Fig. 7.16). The monocline is complicated by minor folding, with the fold axes plunging generally northeast. Due to this secondary bending, the implied general dip changes from roughly northeast to east-northeast in the vicinity of the RSU #1 well (Fig. 7.16). Potential faults identified in vertical sections (Figs. 7.14 and 7.15) appear to correlate with the zone of rapid dip steepening about 1 mi northeast of the well (Fig. 7.16). Based on the contour-line configuration, it is possible to assume that the northwest-striking fault is terminated within the study area by a smaller fault that is roughly orthogonal to the first one.

The principal interpretation objective of this study was to construct a tectonic structural framework that would enable the identification of the faults and fracture

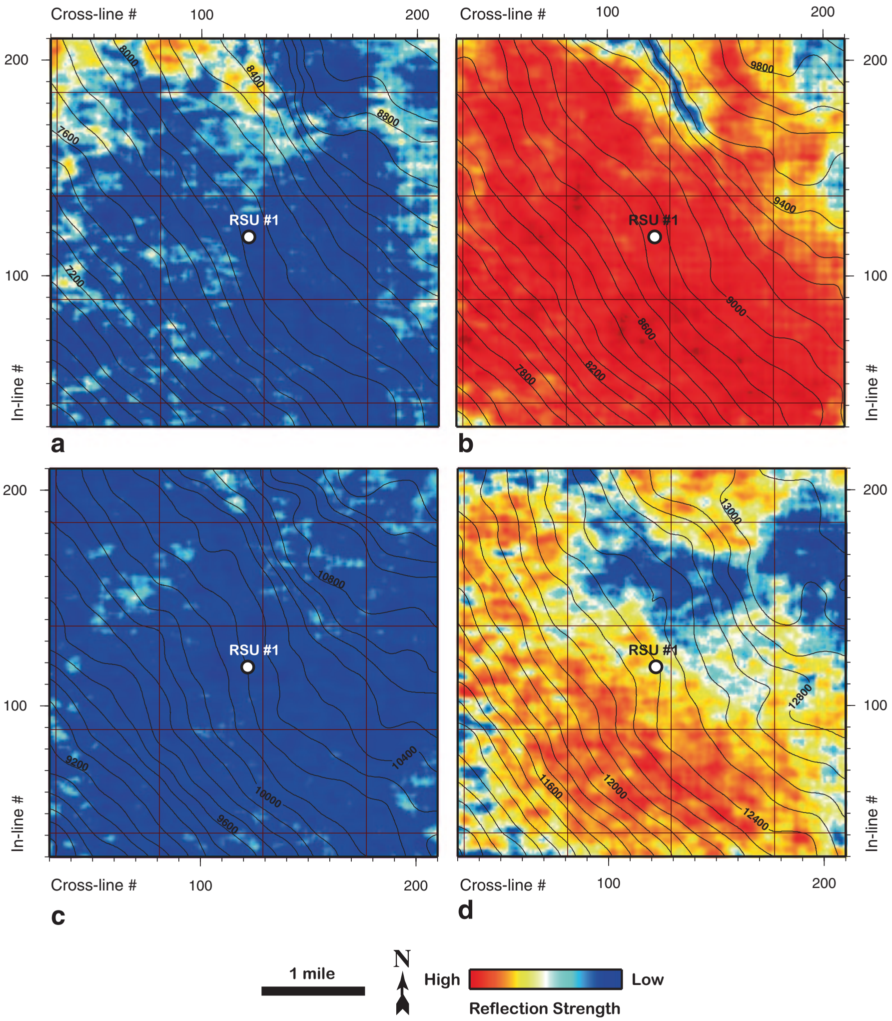

**Fig. 7.17** Reflection strength attribute on top of the following stratigraphic units: (**a**) Mowry, (**b**) Sundance, (**c**) Red Peak, and (**d**) Middle Madison. Reflection strength changes from high (*red*) on interfaces with contrasting physical properties to negligible (*blue*) with seismically transparent, monolithic shale units

network—possible fluid migration pathways. The challenge was to construct this structural picture from a 3-D seismic image that alone could not provide a clear, unambiguous picture of the fault system. Moreover, the seismic data used for structural analysis showed evidence of contamination by an acquisition footprint and processing artifacts arising from irregularities (gaps) in the seismic survey layout, as described in Sects. 7.2 and 7.3 (Figs. 7.1 and 7.3).

Figure 7.17, the reflection strength display, is a phase-independent view of the seismic amplitudes. High reflection strength is commonly associated with major lithologic change (for example, across an unconformity or depositional change), while low reflectivity indicates consistent lithological environment that is more seismically transparent. Observing how reflection strength changes gives us a good idea of how much the lithology is actually changing in three dimensions. For example, relatively low reflectivity can be observed at the top of stratigraphic intervals corresponding to the Mowry Shale and the Red Peak Formation (Fig. 7.17a, c). We interpret these intervals as relatively monolithic and laterally continuous shale units. This is especially true of the Triassic Red Peak Formation, which shows extremely low reflectivity (consistent blue color in Fig. 7.17c). On the contrary, the top of the Sundance Formation is characterized by extremely strong reflectivity, largely due to the Jurassic-Cretaceous disconformity and also to significant impedance contrast between the alternating shales and sandstones composing this stratigraphic interval (Fig. 7.17b). The top of the middle Madison unit shows high reflectivity (Fig. 7.17d) due to the impedance contrast between the high-density limestone unit and underlying porous dolostones. This contrast vanishes northeast (down-dip) of the RSU #1 well but remains laterally consistent to the southwest and west, the up-dip direction (Fig. 7.17d).

The potential faults discussed previously in this section are more readily apparent where the coherence is mapped over the interpreted horizons (Fig. 7.18). Two orthogonal trends were identified in the coherence data. Most of the NW-SE lineations are subparallel to the strike of bedding. The NW-SE lineations seem to terminate at an orthogonal structure in the northeastern corner of the study area (Fig. 7.18). The tracking of these lineations through the coherence volume presented a significant challenge. The difficulty of imaging fault surfaces arises from the local fracture density associated with fault growth (or slip along a fault surface) that produced broad damage zones around the fault planes. Besides, there are plentiful artificial N-S-and E-W-trending lineations associated with the source and receiver layout (acquisition footprint) that intensify the low-reflective horizons. The grid of these artificial (not related to subsurface geology) lineations is especially harmful for the Mowry Shale and the Red Peak Formation images (Fig. 7.18a, c). For the horizons with relatively high reflection strength (Fig. 7.18b, d), the area southwest of the RSU #1 well (the up-dip direction) seems to be laterally continuous and does not contain traceable fault planes.

Other geometrical attributes were analyzed to get a better idea of the geomorphology of the interpreted horizons and also to gain confidence in our fault interpretation. Figure 7.19 shows a set of these attributes extracted at the top of the Sundance stratigraphic interval. Again, the general structure of the region is monoclinal. However, the dip magnitude map (Fig. 7.19a) shows that the attitude of the bedding is not uniform throughout the area. The area northeast of the RSU #1 well is relatively flat (dip 2–6°), but the bedding steepens to dip 6–10° southwest of the well. The RSU #1 well penetrates the Sundance horizon near the northwest-striking bending zone (Fig. 7.19a). Another axis of bed bending can be identified on the dip azimuth map: the regional northeast dip changes to an almost north dip just south of the well (Fig. 7.19b). It looks like the northeast-striking axis of bending changes to a fault axis in the northeastern corner of the survey area. The two orthogonal fault systems become more readily apparent in the two curvature maps (Fig. 7.19c, d).

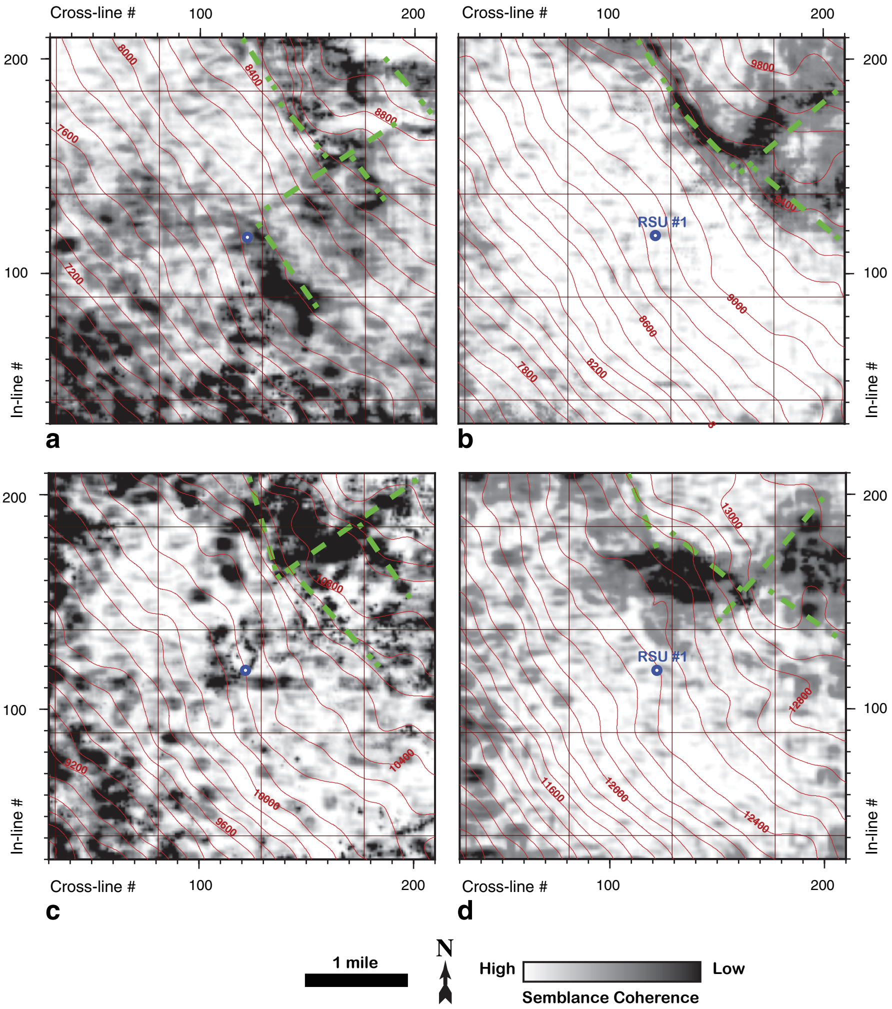

**Fig. 7.18** Interpreted coherence map on top of the following stratigraphic units: (**a**) Mowry, (**b**) Sundance, (**c**) *Red* Peak, and (**d**) Middle Madison. Coherence changes from high (*light color*) in areas with continuous reflections to low (*dark color*) in areas of intense faulting, fracturing, or otherwise poor reflectivity. Interpreted fault axes are shown with *green dashed lines*

The minimum curvature attribute provides better contrast, and the strike curvature allows better resolution of the two faults cutting the strata down-dip (northeast) of the RSU #1 well projection (Fig. 7.19).

The same set of geometric attributes was extracted at the top of the middle Madison stratigraphic interval (Fig. 7.20). The dip magnitude map shows a northwest-striking zone of bending comparable to that interpreted for the Sundance horizon. Although noisier than that of the Sundance horizon, the dip azimuth map of the Madison horizon allows identification of beds bending around an axis that passes

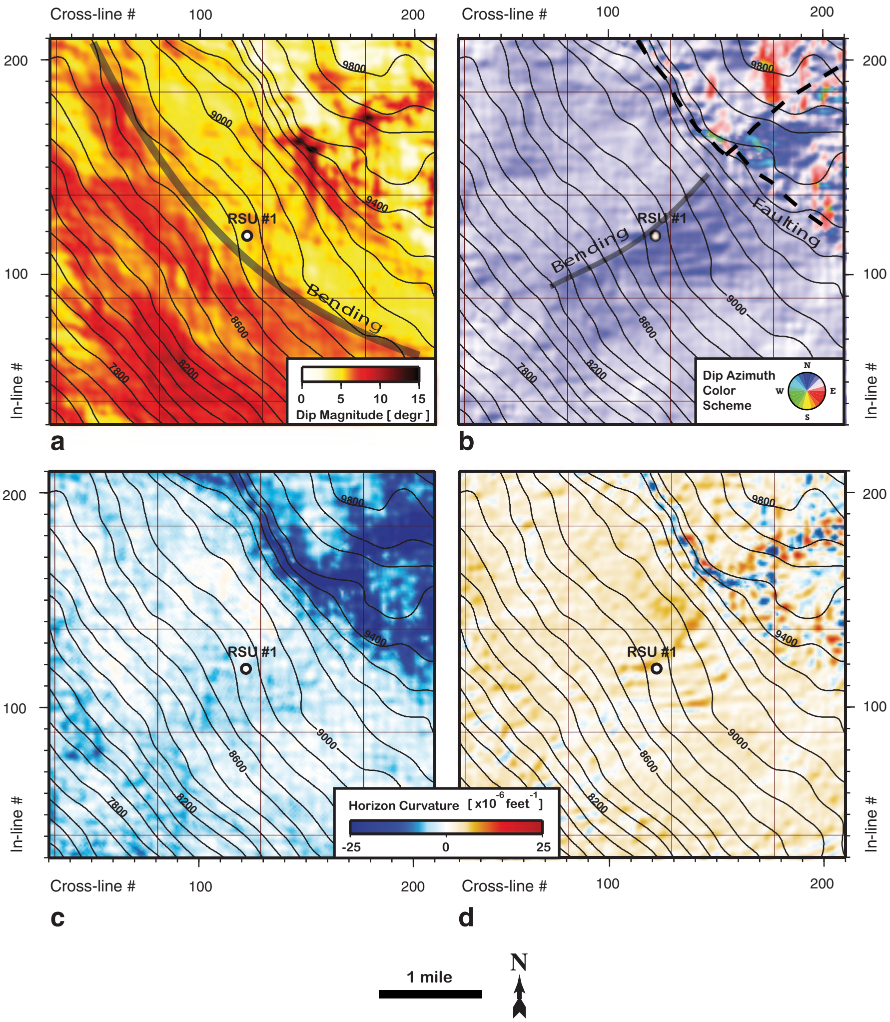

**Fig. 7.19** Geometrical (morphological) attributes on top of the Sundance stratigraphic interval: (**a**) dip magnitude, (**b**) dip azimuth, (**c**) minimum curvature, and (**d**) strike curvature

through the well location (Fig. 7.20b). The northwest-trending fault image, although generally traceable, appears to be more smeared than that on the corresponding Sundance maps. The orthogonal, northeast-trending fault is imaged best in the maximum curvature and dip curvature maps (Fig. 7.20c, d). Compared with those of the Sundance Formation, the northwest-trending structures appear to be shifted up-dip (southwest) on the Madison horizon. This allows us to conclude that both the bending plane and the fault plane dip southwest, which is consistent with our previous interpretation of the vertical coherency sections (Fig. 7.14). The truncated, northeast-trending fault does not greatly change its relative location on the two hori-

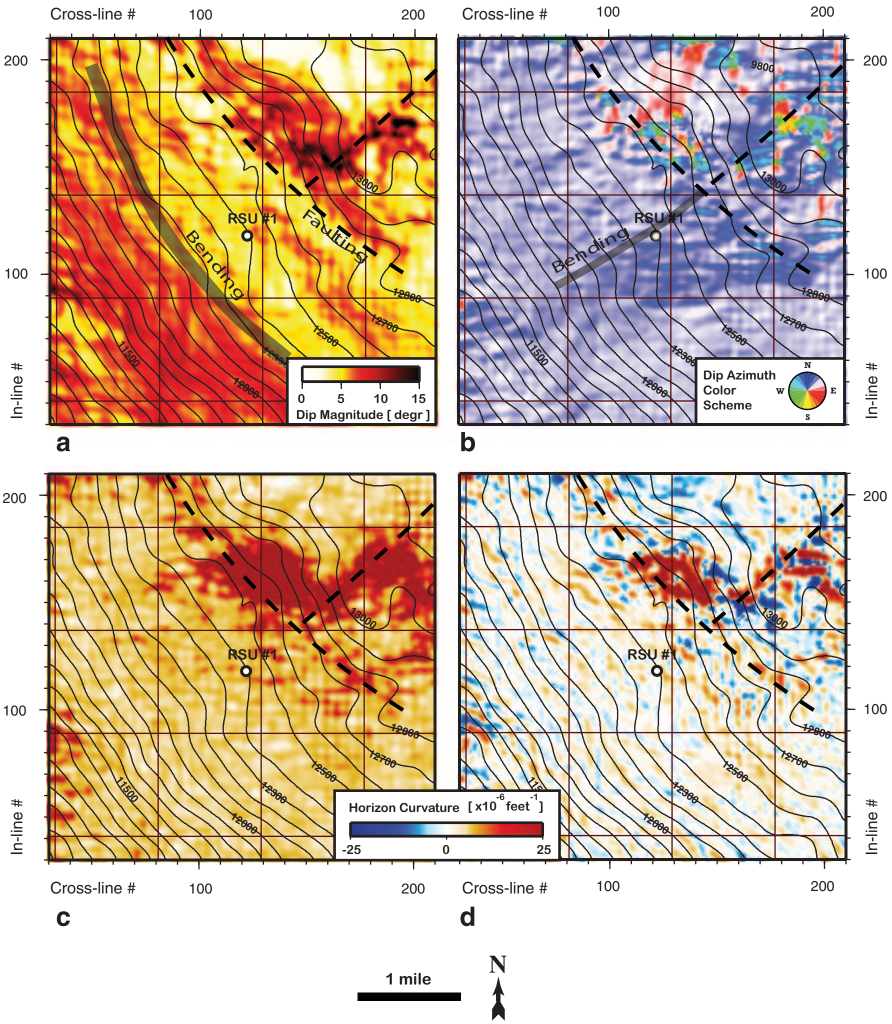

**Fig. 7.20** Geometrical (morphological) attributes along the Madison stratigraphic interval: (**a**) dip magnitude, (**b**) dip azimuth, (**c**) maximum curvature, and (**d**) dip curvature

zons (Figs. 7.19 and 7.20). Hence, at this depth level, the fault plane is sub-vertical. No significant structural complications along the Madison horizon can be observed up-dip of the RSU #1 well; this indicates that the corresponding depth interval is favorable for underground $CO_2$ sequestration.

We used another attribute, mean frequency, to deal with reservoir continuity, compartmentalization, and thickness. We find this attribute to be sensitive to both wave propagation effects and depositional characteristics. Its uses within the study area included:

- Fault/fracture zone indication. Fractures may appear as lower-frequency zones.

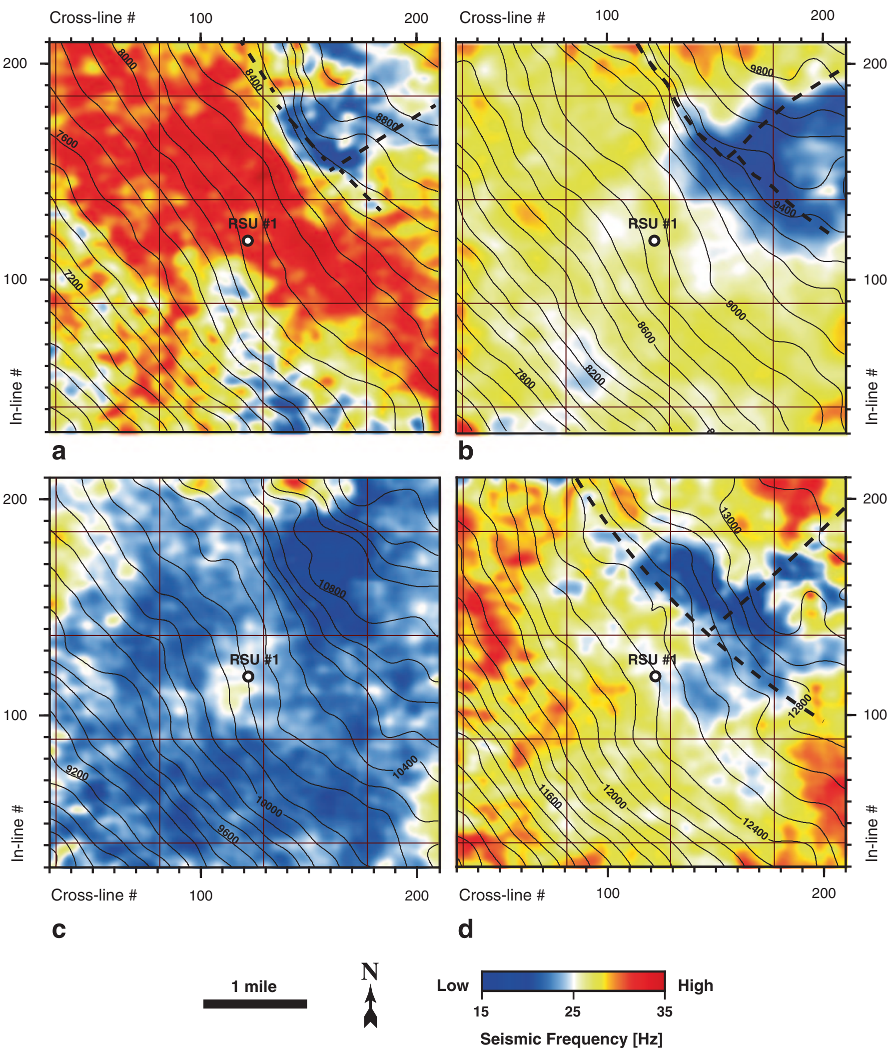

**Fig. 7.21** Mean frequency attribute on top of the following stratigraphic units: (**a**) Mowry, (**b**) Sundance, (**c**) *Red* Peak, and (**d**) Middle Madison. Frequency varies from high (*red*) to low (*blue*)

- Bedding characterization. Higher frequencies indicate the presence of sharp interfaces such as exhibited by thinly laminated shales or complex depositional systems composed of alternating lithologies. Lower frequencies are indicative of relatively monolithic units (e.g. sandstones) with more massive bedding geometries.
- Bed thickness mapping. A reflection from a thin bed has a characteristic expression in the frequency domain that is indicative of the temporal bed thickness. A "thin bed" is indicated where the two reflected waveforms from the top and base of the layer interfere.

**Table 7.3** Seismic modeling parameters

| Modeling unit | Density (g/cc) | P-wave velocity (ft/s) |
|---|---|---|
| Reservoir rocks | 2.52 | 18,000 |
| Encasing rocks | 2.72 | 21,000 |

Figure 7.21 shows mean frequency maps on top of several representative horizons. The Mowry Shale interval, composed of thinly laminated and fractured lithologies, is imaged with high frequencies (red in Fig. 7.21a). The Sundance Formation also appears to be composed of alternating lithologic units with contrasting physical properties, but shales of the Red Peak Formation are mapped as uniform monolithic strata (Fig. 7.21b, c). The broad zone of intense fracturing northeast of the RSU #1 well is consistently imaged with low frequencies. A noticeable acoustic impedance contrast characterizes the middle Madison reservoir unit enclosed within massive carbonate rocks. That is why the frequency distribution map over this stratigraphic interval is mostly composed of high frequencies (red and yellow in Fig. 7.21d).

Forward modeling was performed to examine the physical basis for links between the varying thickness of the middle Madison unit and several seismic attribute responses. We modeled the seismic response to varying thickness on a wedge that mimics the middle Madison unit (Fig. 7.22a). The density and velocity values used in the modeling are loosely based on physical properties of the middle Madison reservoir rocks encased in acoustically dissimilar carbonates (Table 7.3).

To represent the petrophysical profile of the Rock Springs Uplift, we assumed that the porous dolostone wedge is lower in acoustic impedance than the surrounding material. Correspondingly, the top and bottom of the wedge show opposite reflection polarities, which is a realistic and common situation in most stratigraphic profiles with reservoir rocks (Fig. 7.22a). The wedge thickens in value from zero on the left to 600 ft on the right, which corresponds to one dominant wavelength ($\lambda$) at the reservoir depth. The geologic model was convolved with the zero-phase Ormsby wavelet (limited by 4-, 8-, 48-, and 80-Hz cutoff frequencies) to produce a simple, zero-offset acoustic model of the seismic response of the wedge. Based on the vertical resolution limit ($\lambda/4$), the model covers a thickness range from seismically thin beds ($<\lambda/4$) through intermediate beds ($\lambda/4$–$3\lambda/4$) to seismically thick beds ($>3\lambda/4$). From the well-log measurements, the middle Madison reservoir thickness at the RSU #1 well site is 140 ft, which is close to $\lambda/4$. Figure 7.22a shows rows of antisymmetric waveforms that correspond to the top and bottom of a porous dolostone reservoir of varying thickness. For seismically thin and intermediate beds, reflection amplitudes are composite seismic responses resulting from the interference of the top and bottom reflections.

The corresponding amplitude and frequency values measured from the seismic response are shown in Fig. 7.22b, c. The amplitude curve is characterized by a maximum value (called *tuning*) at approximately $\lambda/5$, which is the tuning thickness in our case. As the wedge thins to less than $\lambda/5$, the amplitude begins a sharp decrease to zero. Although such nonlinear changes in seismic amplitude are well-established effects of thin-bed tuning, the corresponding changes in seismic signal frequency are much less

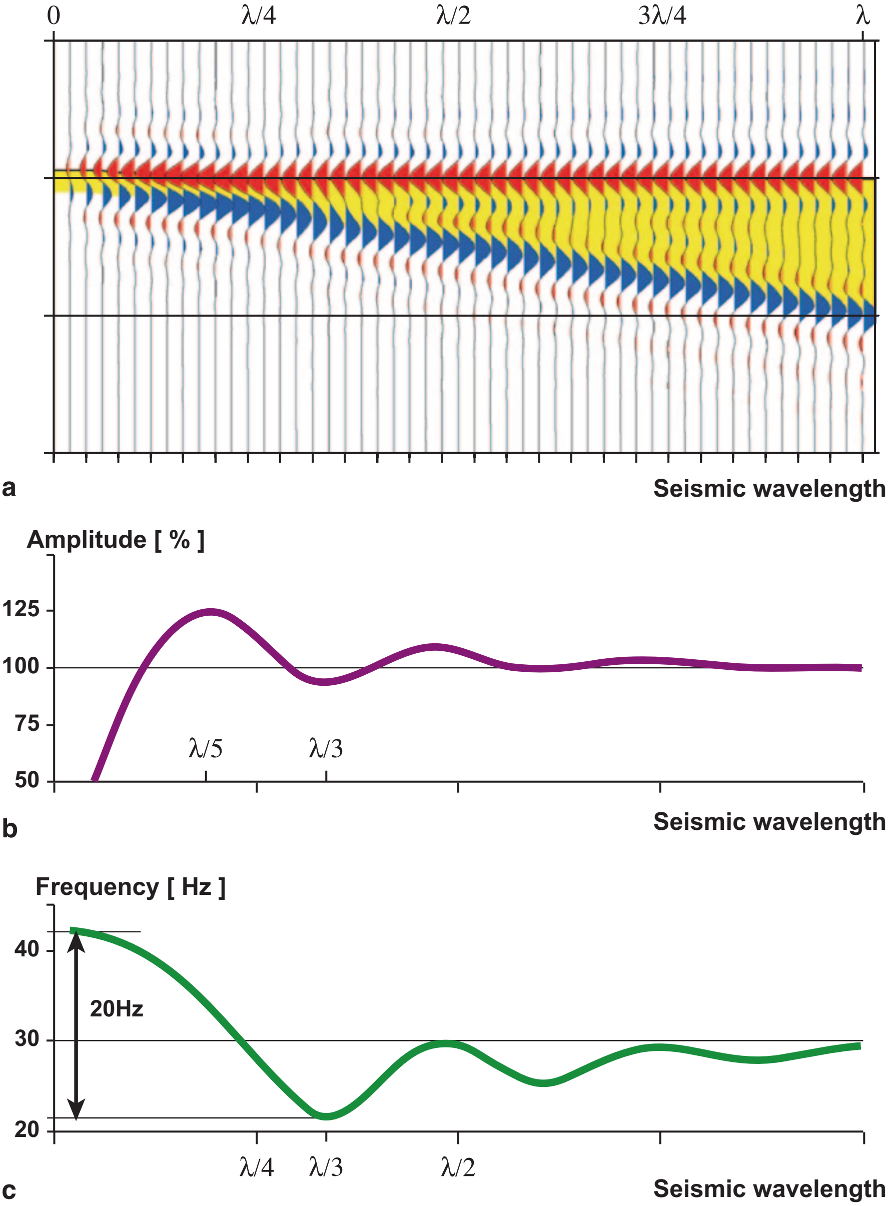

**Fig. 7.22** (**a**) Low-impedance wedge model (*yellow*) and its seismic response generated using zero-phase Ormsby wavelet with frequency passband 8–48 Hz. (**b**) Amplitude and (**c**) mean frequency variations estimated on top of the wedge

well documented. In this study we attempted to fill the gap by calculating the mean frequency of the spectrally decomposed reflection that corresponds to the top of the wedge. The frequency-tuning curve (Fig. 7.22c) demonstrates generally oscillating

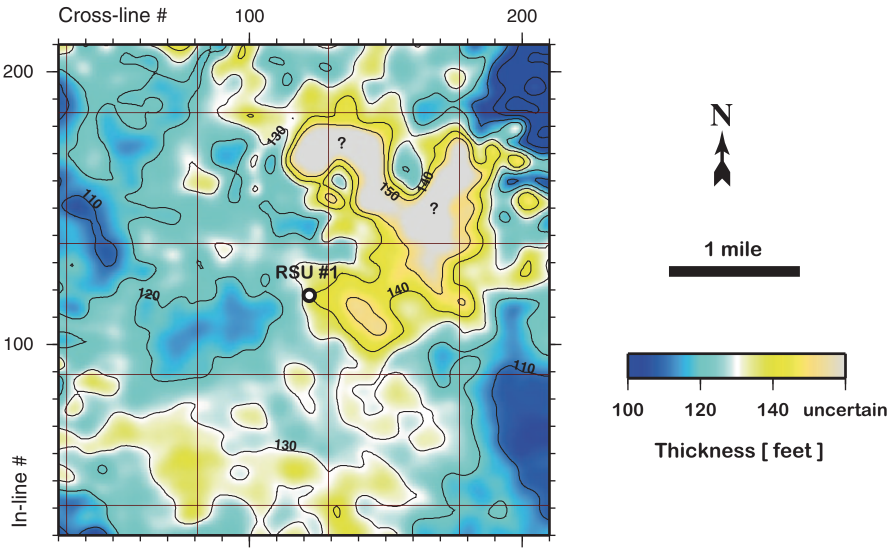

**Fig. 7.23** Color-coded isopach map of the middle Madison reservoir. The reservoir thickness varies from ~110 ft (*blue*) to ~140 ft (*yellow*). Areas with increased uncertainty (possible faulting) are grayed-out

behavior around an average wavelet frequency of 30 Hz. The most important changes in frequency occur from zero to $\lambda/3$ (approximately 200 ft for the model parameters) where the wedge thickens. This interval is characterized by a corresponding decrease in frequency (of approximately 20 Hz). The inversely proportional behavior of the frequency-tuning curve for beds with thickness below $\lambda/3$ is utilized in this study.

The inversely proportional dependence of seismic frequency on thickness for beds thinner than one-third dominant seismic wavelength is not a result of specific modeling parameters. The authors tested wedge models of the embedded layer with both positive and negative impedance contrasts. The authors also analyzed the frequency response of the wedge model produced by 90°-phase wavelets with different average frequencies. The modeling results indicate that, in all cases, the lowest measured frequency corresponds to the wedge thickness equivalent to $\lambda/3$.

To check the applicability of the mean frequency attribute as bed-thickness discriminator, we routinely computed the middle Madison reservoir thickness by measuring the corresponding peak-trough separations within the seismic volume. The resultant isopach map is shown as Fig. 7.23. Within the study area the reservoir thickness varies from about 110 ft to about 140 ft. Except in areas affected by faulting or acquisition footprints or both, the middle Madison isopach map (Fig. 7.23) shows a strong correlation with the frequency distribution over the corresponding reflection horizon (compare Fig. 7.23 with Fig. 7.21d).

Areas where the reservoir thins to less than 120 ft (Fig. 7.23) correspond to high-frequency build-ups in the mean frequency attribute map on top of the middle Madison reservoir (Fig. 7.21d). On the contrary, an increase in reservoir thickness (e.g. southeast of the well, Fig. 7.23) manifests lowering frequency content. Thus, two

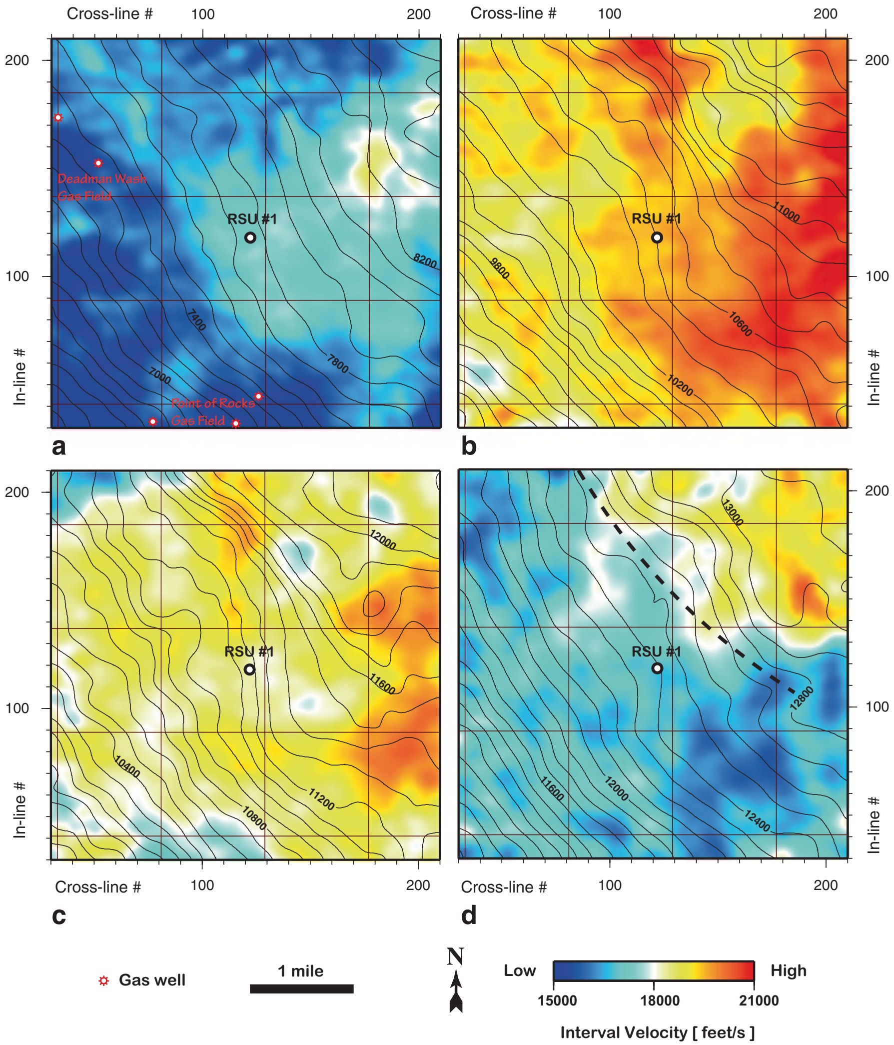

**Fig. 7.24** Velocity attribute on top of the following stratigraphic units: (**a**) Frontier, (**b**) Dinwoody, (**c**) Weber, and (**d**) middle Madison. Velocity varies from high (*red*) to low (*blue*)

different approaches used for reservoir thickness characterization appear to produce comparable results. This gives us greater confidence in the isopach map, Fig. 7.23.

The velocity attribute maps shown in Fig. 7.24 actually represent interval velocity models obtained from reflection seismic data. These interval velocities were measured using a standard semblance method and the well-known Dix formulation (Dix 1955). As in any modeling, our degree of confidence in identified features and their associated interpretation depends on the density of the modeled data set. In this study, our semblance measurements are sampled densely, 110 ft×110 ft×2 ms, and that makes our velocity models more precise (and probably more accurate) than those models

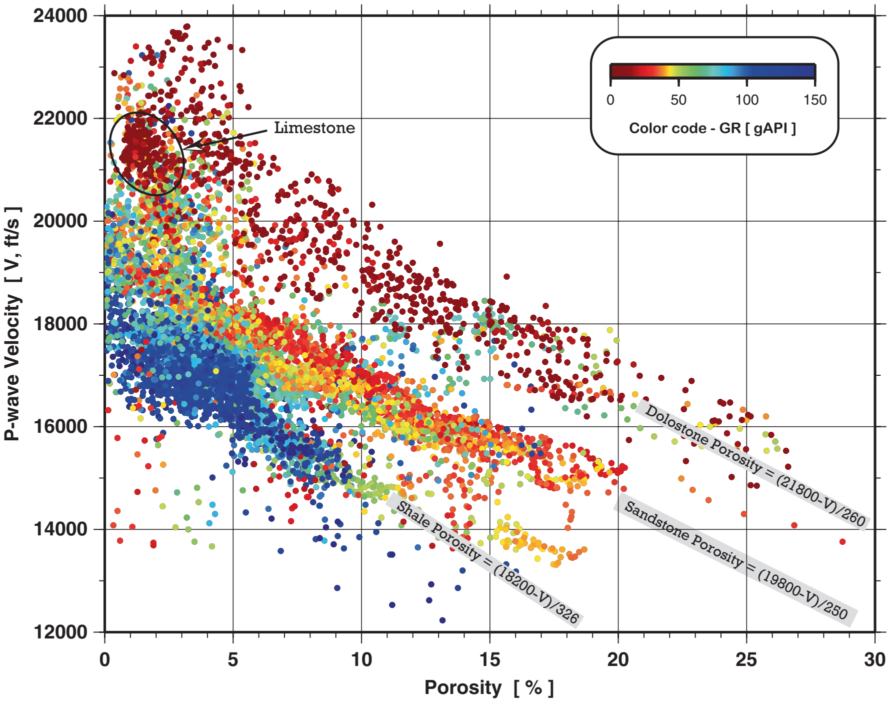

**Fig. 7.25** Sonic P-wave velocity versus density porosity crossplot color-coded with the gamma ray log data. The measured depth interval is from 8,600 to 12,700 ft (pre-Cretaceous strata). Interpreted lithologies and the corresponding linear regression models are shown within the *gray* bars

produced for conventional stacking purposes. In standard templates, semblances are commonly sampled coarsely and then smoothed, resulting in a loss of valid information and resolution. Consequently, the information illustrated on the horizon velocity distribution maps (Fig. 7.24) is commonly unavailable to the interpreter.

Unlike velocity-time profiles, such as that shown in Fig. 7.10, velocity distribution maps (Fig. 7.24) do not exhibit abrupt changes, and the range of lateral velocity variation for most interpreted horizons does not exceed 4,000 ft/s. Since velocity variations are known to commonly correlate well with lithology that remains constant along a seismic horizon, these results are what we would expect. Heterogeneous lithologic characteristics of subsurface formations are manifested mostly by vertical variations in velocity, while lateral velocity variations can be attributed to variable porosity, fracturing, and fluid content. Therefore, we interpret velocity trends observed in lateral subsurface images mostly in terms of porosity and hydrocarbon accumulation.

The first velocity distribution map over the Frontier horizon (Fig. 7.24a) illustrates this interpretation: seismic interval velocities can be used to detect the extent of gas-saturated formations. Low velocity zones are associated with the two prolific gas fields (Fig. 7.24a). The hydrocarbon bearing zones west (Deadman Wash gas field) and south (Point of Rocks gas field) of the RSU #1 well correlate with intense low-velocity anomalies.

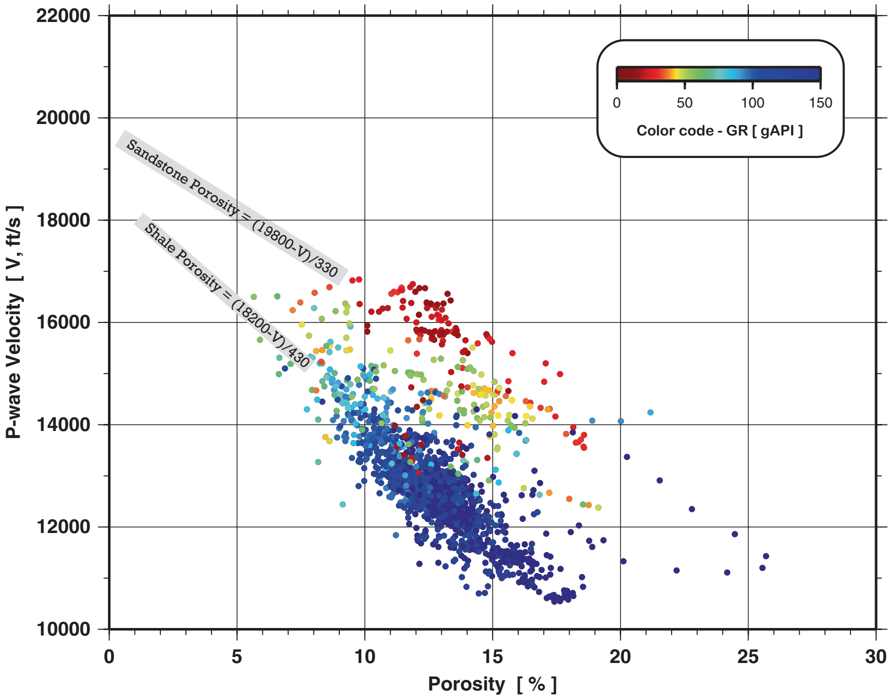

**Fig. 7.26** Sonic P-wave velocity versus density porosity crossplot color-coded with the gamma ray log data. The measured depth interval is from 7,700 to 8,500 ft (Cretaceous Dakota through Frontier Formations). Interpreted lithologies and the corresponding linear regression models are shown within the *gray* bars

Stratigraphically lower horizons, the Dinwoody and the Weber, are characterized by relatively uniform velocity distribution and a higher range of values, 18,500 ft/s to about 20,500 ft/s. There is only a weak trend of velocity decrease west of the test well location on these two horizons (Fig. 7.24b, c). The middle Madison unit (Fig. 7.24d), the deepest interpreted stratigraphic horizon, is distinguished by low overall velocity values (16,000–19,000 ft/s) and strong lateral velocity variations, which may be associated with complex overburden structures.

We used geophysical logs from the RSU #1 well [ESM plate 6] to gain insight into velocity variations along these four horizons (Fig. 7.24). The gamma ray, sonic, density, and neutron porosity log characteristics were used in the correlation analysis. Density porosities were derived assuming a multi-component mineral mixture with variable matrix densities that were interpreted from the neutron/density crossplot. The resultant velocity-porosity relationships were estimated from regression methods that fit linear trends for the intervals identified in Figs. 7.25 and 7.26. On the basis of these petrophysical relationships, and considering negligible lithological variation along the interpreted seismic horizons, we predicted the porosity distribution along the four horizons shown in Fig. 7.27. As expected, the gas fields producing from the Frontier Formation are located over the high-porosity areas (Fig. 7.27a). The Weber Sandstone can be characterized as a tight reservoir,

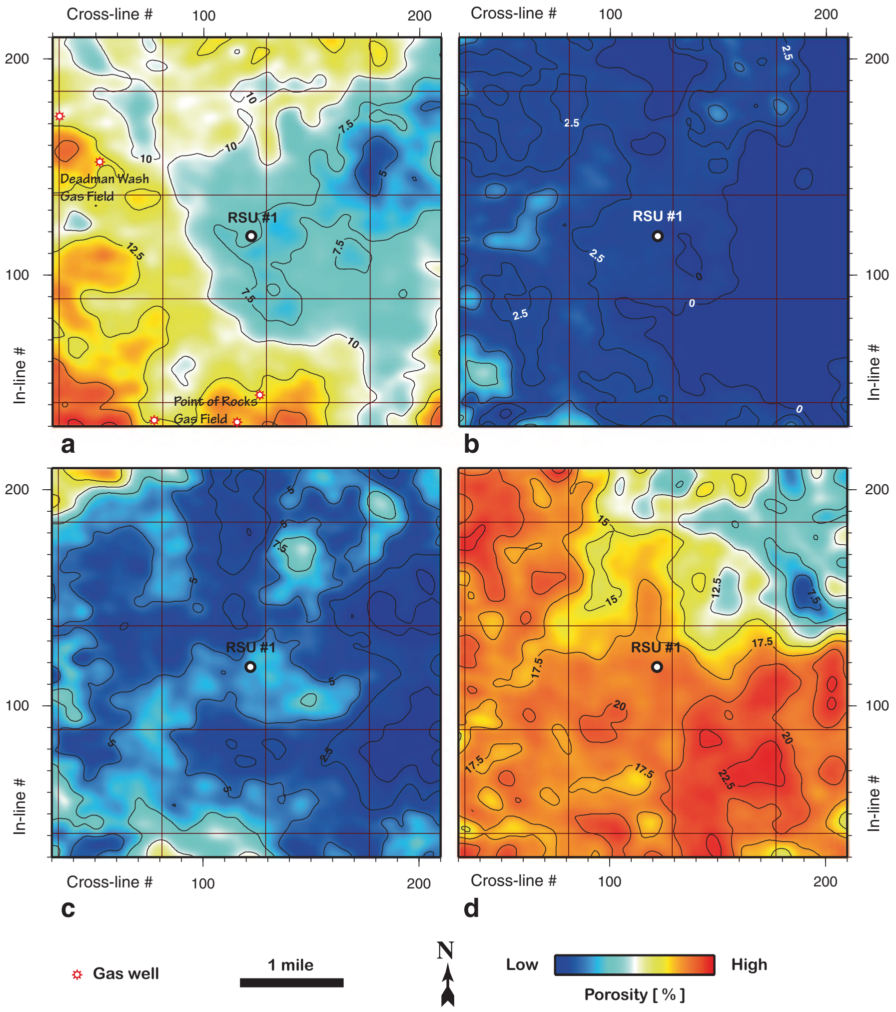

**Fig. 7.27** Porosity maps on top of the following stratigraphic units: (**a**) Frontier, (**b**) Dinwoody, (**c**) Weber, and (**d**) middle Madison. Porosity varies from high (*red* color) to low (*blue* color). Contour lines indicate porosity with contour interval = 2.5 %

with porosities ranging from 5 to 10 %. The middle Madison unit (Fig. 7.27d) looks very promising for $CO_2$ sequestration on the basis of consistently high (greater than 15 %) porosities in the up-dip direction. The integrity of the sealing horizon is verified by extremely low (less than 5 %) porosities on the top of the Dinwoody Formation (Fig. 7.27b), which overlies the targeted reservoir formations.

## 7.11 Qualitative Permeability from Seismic Attribute Analysis

### *7.11.1 Modeling the Seismic Signature of Permeable Layers*

Permeability and porosity are key inputs into reservoir flow simulation. If an impedance-porosity transform is available, porosity can be inferred from acoustic impedance. Such transforms can be derived from sonic, density, and porosity data from well logs. Typically, a theoretical rock physics model is found to explain these data and then used to expand the impedance-porosity interpretation away from the well by the means of inverted seismic data. However, permeability, which is necessary for reliable reservoir modeling, seems to be the most elusive of reservoir properties and remains extremely uncertain.

In this section, we examine the detection of permeable conduits that are important in fluid migration through the fractured, dual-porosity carbonates. *Dual-porosity* rocks are rocks that have both matrix porosity (primary porosity) and fractures (secondary porosity). In dual-porosity rocks, the bulk permeability is provided by fractures or vugs connected with each other and with high-aspect-ratio intergranular pores.

Natural rock reservoirs, including carbonates, are fluid-saturated, porous materials whose elastic properties can be described by Biot's (1962) poroelastic theory. Biot's theory predicts pore-fluid motion relative to the solid rock matrix during the passage of seismic waves through rocks. The corresponding energy loss arising from relative fluid motion is also evaluated. Importantly, Biot's theory gives an opportunity to estimate fluid and rock transport properties by measuring seismic amplitude. Recent studies (Pride et al. 2003; Goloshubin et al. 2008; Kozlov 2007; Ren et al. 2009) found that permeability can affect seismic reflection amplitudes significantly, especially for reservoirs built of layered porous material with heterogeneous permeability distribution.

In general, reflection-coefficient equations for dispersive media are very complicated. However, they can be simplified for normal incidence. For example, Goloshubin and Silin (2006) provide simple expressions for reflection and transmission coefficients for a planar P-wave from a permeable boundary in a fractured reservoir. Goloshubin et al. (2008) derive the reflection coefficient equation for the case of an inhomogeneous reservoir consisting of *N* permeable lenses. The important feature of this equation is that it accounts for the dependence of the reflected signal on the frequency. This provides the basis for the spectral decomposition technique to be a powerful tool in estimating reservoir transport properties.

Since the middle 90s, various seismic attributes have been proposed for mapping permeability by using detailed analysis of the reflected-waveform amplitude spectra. These attributes are calculated by using a sort of spectral decomposition technique first introduced for seismic interpretation by Morlet et al. (1982) and substantially developed by Partyka et al. (1999). According to Castagna and Sun (2006), spectral decomposition in seismic exploration is a method that produces a continuous time-

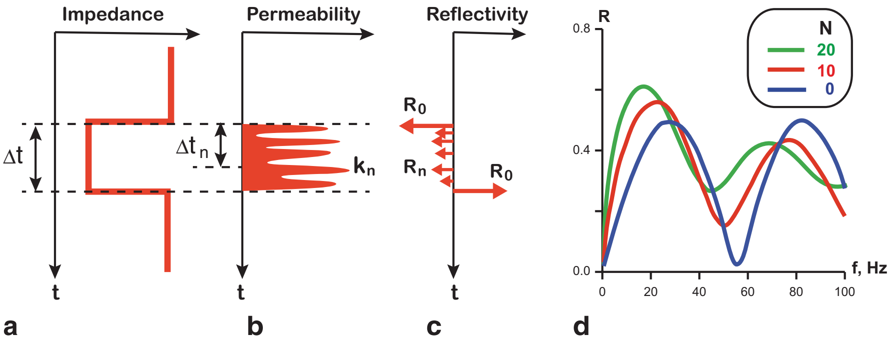

**Fig. 7.28** Reservoir model of a low-impedance layer (**a**) with high-permeability lenses (**b**) and the model response on incident P-wave (**c**): $R_0$ are reflection responses from reservoir's top and base, $R_n$ are responses from the lens n, Δt is time thickness of the reservoir, and $\Delta t_n$ is time delay of the seismic response from lens n. Reflection coefficient R from the modeled reservoir as a function of number of lenses N and seismic frequency f (**d**). (All figures modified from Goloshubin et al. (2008))

frequency expression of a seismic trace. Applying instantaneous time-frequency analysis to seismic data makes it possible to compute various permeability-dependent attributes. For example, one group of attributes maps the ratio of the high-frequency part of the amplitude spectrum of a seismic trace to the low-frequency part. Other attributes make use of the slope characteristics of the low- and high-frequency parts. Some permeability attributes demonstrate a relative increase in high-frequency content with increased permeability; other attributes show the opposite. Kozlov (2007) found that for dual-porosity reservoirs consisting of thin, alternating permeable and impermeable layers, the permeability attributes become ambiguous because the frequency dependence of the reflectivity function is strongly affected by layering. Even for a single permeable layer encased within impermeable rock, the permeability attributes can be either directly or inversely proportional to frequency, depending on the layer thickness expressed in the dominant seismic wavelength (Kozlov 2007). Hence, it is important to consider the geometry of a heterogeneous reservoir (thickness and layering) in modeling its comparative permeability.

As derived by Goloshubin et al. (2008), in the case of a normal-incident P-wave reflected from an inhomogeneous reservoir with *N* permeable lenses (see Fig. 7.28a, b, c for the model delineation), the reflection coefficient $\boldsymbol{R}(\omega)$ approximates to:

$$\boldsymbol{R}(\omega) \approx \boldsymbol{R}_0 - \left(1 - \boldsymbol{R}_0^2\right)\boldsymbol{R}_0 e^{-\mathrm{i}\omega\Delta t - a(\omega)} + \sum_{n=1}^{N} \boldsymbol{R}_n \sqrt{\left(\frac{\mathrm{i}\omega\rho_\mathrm{f}\mathrm{k}_\mathrm{n}}{\eta}\right)}\, e^{-\mathrm{i}\omega\Delta t_n - a_n(\omega)}, \tag{7.7}$$

where $\omega = 2\pi f$ is the angular frequency, $R_0$ is the reflection coefficient from the top of the reservoir, $\mathrm{i} = \sqrt{-1}$, $\Delta t$ is the two-way travel-time thickness of the reservoir, $\alpha(\omega)$ describes transmission and absorption energy losses from a P-wave reflected from the base of the reservoir, $R_n$ is the reflection coefficient from the nth lens, $\rho_f$ and $\eta$ are the pore-fluid density and viscosity, $k_n$ is the rock permeability of the nth lens, and $\Delta t_n$ and $\alpha_n(\omega)$ are time delay and transmission-absorption losses for the seismic response from lens *n*.

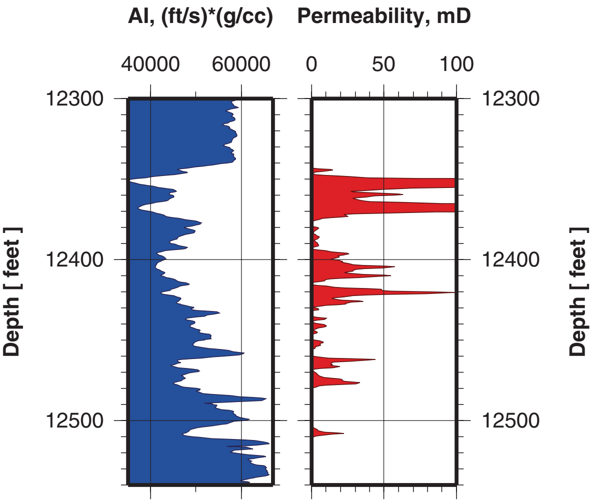

**Fig. 7.29** Acoustic impedance (*AI*) and permeability data derived from the Madison Formation logs in the RSU #1 well. The Middle Madison rocks (from 12,340 to 12.510 ft depth) are dual porosity carbonates characterized with interlayered zones of increased fracturing and permeability (vuggy dolostones) and zones of prevailing microporosity having high impedance and low permeability

Figure 7.28d shows the behavior of the fluid-saturated reservoir reflectivity as a function of seismic frequency $f$ and the number of reservoir layers $N$ having variable permeability $K_n$. There is a significant shift of the first reflected amplitude peak toward lower frequencies. The effect of increased reflectivity at lower frequencies progressively smoothens as the number of high-permeability lenses is increased. However, even with the number of layers $N = 20$, the low-frequency ($f = 20$ Hz) reflectivity is twice as great as the high-frequency ($f = 40$ Hz) reflectivity (Fig. 7.28d). This suggests that spectral analysis of a seismic reflected signal can be used to discriminate reservoirs with dual-porosity—having intense fracturing or vuggy porosity development with associated zones of high fluid mobility—from low-permeability reservoirs with intergranular porosity only. Provided the reservoir modeled in Fig. 7.28 does not have significant thickness variations, we can expect a strong amplitude resonance effect resulting from high-permeability lens development but a uniform distribution of reflectivity with frequency resulting from a low-permeability reservoir.

## *7.11.2 Qualitative Permeability of the Middle Madison Reservoir*

Acoustic impedance and permeability data derived from the Madison Limestone logs in the RSU #1 well demonstrate close resemblance of the Madison to the dual-porosity reservoir modeled in Fig. 7.28. At the RSU #1 well site, impermeable carbonates enclose the dual-porosity, low-impedance, vuggy dolostones of the middle Madison unit between depths of 12,340 and 12,510 ft (3,761 and 3,813 m) (Fig. 7.29). The middle Madison rocks show a high degree of vertical heterogeneity, with permeability variations of several orders of magnitude. About a dozen highly permeable zones within the middle Madison have permeability of more than 10 mD (Fig. 7.29). The alternating permeable and impermeable layers within the middle Madison reservoir match conditions of low-frequency resonance in seismic reflectivity (Fig. 7.28). This leads us to propose that spectral decomposition of reflection seismic data is an effec-

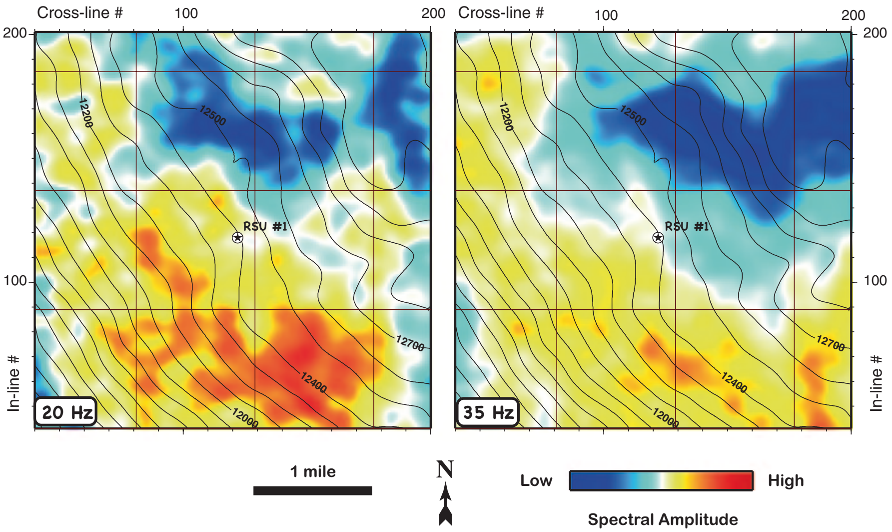

**Fig. 7.30** Middle Madison amplitude slices extracted from the spectrally decomposed volumes: 20-Hz isofrequency amplitude (*left* panel), 35-Hz isofrequency amplitude (*right* panel). Labeled structure contour lines represent depth (ft) below KB at the RSU #1 well

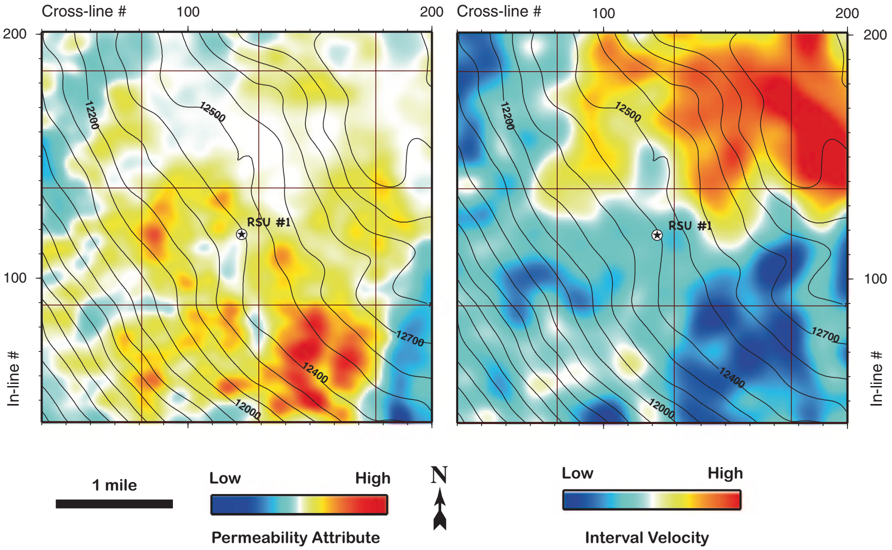

**Fig. 7.31** Color-coded permeability attribute (*left* panel) and interval velocity (*right* panel) maps calculated on top of the Middle Madison horizon. Note that high-permeability area southeast from the RSU #1 well correlates with low-velocity zone. Labeled structure contour lines represent depth (feet) below KB at the RSU #1 well

tive tool for mapping lateral variations of permeability within the middle Madison rocks. According to Kozlov (2007), a decrease of P-wave velocity is another essential aspect of the seismic signature of permeability increase in the case of dual porosity.

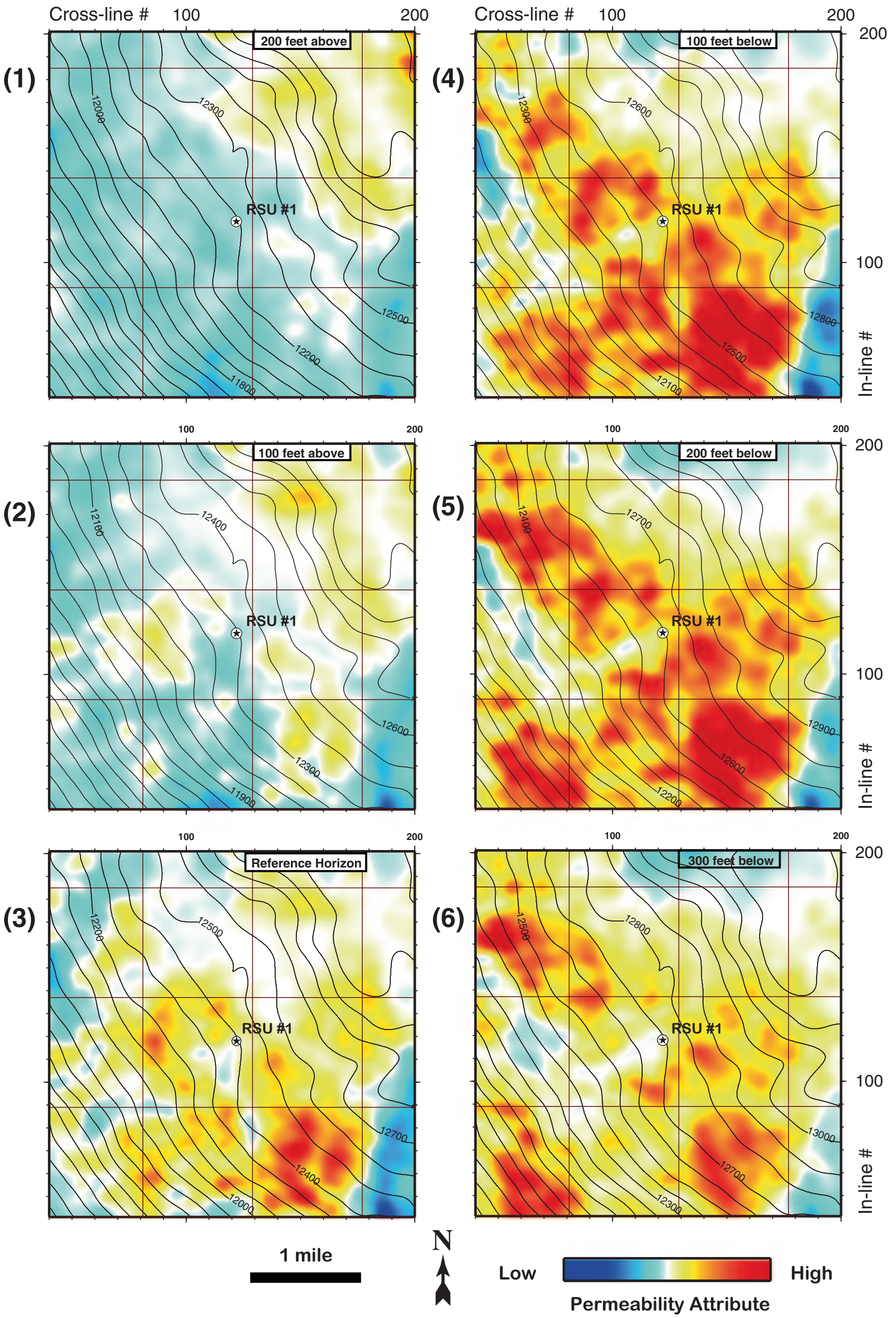

**Fig. 7.32** Color-coded permeability attribute maps calculated along the Middle Madison phantom horizons: (*1*) 200 ft above the reference horizon, (*2*) 100 ft above, (*3*) on top of the Middle Madison, (*4*) 100 ft below the reference, (*5*) 200 ft below the reference, (*6*) 300 ft below the reference horizon. Contour lines represent depth below KB of the corresponding phantom horizons

Figure 7.30 compares two frequency slices corresponding to the middle Madison reflection horizon, extracted from spectrally decomposed volumes; Fig. 30a corresponds to the low-frequency (20 Hz) response, while Fig. 30b shows the reflectivity of the middle Madison horizon at a relatively high frequency (35 Hz). The area northeast of the RSU #1 well is characterized by low reflectivity at both frequencies, while south and west of the well the seismic reflected signal exhibits high amplitudes. This can be explained by increased noise content due to the Jim Bridger power plant located about 1 mi northeast of the RSU #1 well. Considering possible noise originating at the power plant, we designed a *permeability attribute* that is proportional to the difference between the low-frequency spectral amplitude along the middle Madison reflection horizon and the high-frequency spectral amplitude, and is scaled by the sum of the two components. Thus, the areas with high noise content appear to be more attenuated on the permeability attribute maps.

The permeability attribute described above is shown in Fig. 7.31a. Relative variations of this attribute are proportional to the weighted average permeability within the middle Madison reservoir. This statement finds support in Fig. 7.31b, which shows the seismic interval velocity distribution on the top of the middle Madison horizon. There is noticeable correlation between the high-permeability area southeast of the RSU #1 well and the low-velocity anomaly at the same location.

Permeability attribute maps were calculated for several phantom horizons, conformal to the *reference middle Madison horizon*. The maps in Fig. 7.32 allow estimation of the volumetric permeability distribution within the reservoir rocks. The maximum permeability attribute anomaly (corresponding to low-frequency amplitude resonance) is mapped at 100 and 200 ft below the reference horizon (Fig. 7.32d, e) and appears decayed 300 ft below the reference horizon (Fig. 7.32f). On the basis of the seismic data, the middle Madison reservoir is thus at least 100 ft thick. Immediately above the reference horizon, within the upper Madison unit (Fig. 7.32a, b), the permeability attribute appears to have much lower values (corresponding to high-frequency amplitudes resonance) and a much more uniform distribution. At the RSU #1 well location the thickness of the middle Madison unit is 160 ft (Fig. 7.29), which agrees well with the seismically derived permeability attribute distribution. These comparative permeability distribution maps (Fig. 7.32) were computed with the objective of increasing the accuracy of flow simulation for the middle Madison reservoir.

## Glossary of Seismic Terms

**Acquisition** the generation of seismic energy waves within the earth and their distant recording.

**Acquisition footprint** any regularity or pattern in seismic data that is not of geologic origin and can be due to acquisition or processing problems.

**Aliasing** an effect that causes some continuous signals to become indistinguishable when sampled.

**Azimuth** angle measured clockwise from north to a linear direction.

**Bin** an area on the land surface that captures any seismic trace whose midpoint falls into it. All the traces in a bin form a three-dimensional CMP gather.

**Common gather** a collection of seismic traces with a common or fixed characteristic. For example, a common shot gather is all traces generated by the same shot.

**Component** the directional orientation of a source or receiver during acquisition. Conventional surface seismic involves data recording in one vertical component and two horizontal components.

**CMP** (1) literally, common midpoint. The midpoint surface location for a seismic trace that is calculated from source and receiver coordinates. (2) A seismic acquisition and processing technique that yields multiple prestack traces at each midpoint location.

**CMP fold** the number of traces in a CMP gather. Conventional processing involves summation (stacking) of these traces to produce one poststack trace.

**CMP gather** gather of all traces in a seismic survey having the same midpoint number or bin.

**CMP stack** a stack of all prestack traces associated with the same midpoint number or bin.

**Depth structure map** a map in depth units that is generated from a time structure map by means of a time-depth transform function.

**Far offset** the distance from source to farthest receiver.

**Fold** the number of seismic traces within a gather.

**Frequency** the number of wave peaks or cycles per second.

**Gather** see Common gather.

**Horizon slice** a horizontal display or map view of 3-D seismic data showing a particular reflection, as opposed to a time slice that has a constant travel time.

**Interface** a surface in the earth where velocity, density, or other physical parameters change abruptly. Commonly, but not necessarily, coincident with a change in rock type or pore fluid.

**Interpretation** the analysis of geophysical data to generate geologicly reasonable models and predictions about subsurface properties and structures.

**Inversion** (1) a process of estimating subsurface physical parameters (velocity, density, etc.) from seismic data. (2) A situation where a low-velocity layer underlies a high-velocity layer.

**Lateral resolution** the minimum separation of two features in map view before their individual identities are lost.

**Medium** a term designating a specific location (layer or section) within the layered earth model. Plural is media.

**Midpoint** the point on the land surface halfway between source and receiver.

**Migration** the process by which seismic events are geometrically re-located in either space or time to provide a more accurate image of the subsurface.

**Offset** the distance between the source and receiver associated with a trace.

**Phantom horizon** a seismic attribute not coincident with a certain tracked horizon but conformal to it and shifted by a certain number of milliseconds.

**P-wave** the primary or fastest wave traveling away from a seismic energy source. This kind of seismic wave excites particle motion that is parallel to the direction of wave propagation. Currently, this is the main wave type used in reflection seismology.

**Poststack** an object or process related to seismic data after CMP stacking.

**Prestack** an object or process related to seismic data before CMP stacking.

**Processing** a sequence of digital data processing routines followed to enhance reflected seismic signals and to suppress noise.

**Receiver** a device for measuring surface motion due to the passage of seismic or sound waves.

**Reflected wave** the wave that returns back to the surface after reflection from an interface.

**Reflection** (1) the process in which a seismic wave strikes and partially bounces off an interface. (2) An event recorded on the surface as a seismic image (in section or map view) associated with reflection from a particular interface.

**Reflection coefficient** the ratio of the amplitude of a reflected wave to the amplitude of the incident wave.

**Reflection coefficient series** the reflection coefficient as a function of recording time (depth).

**Reflector** the interface associated with a particular reflection event.

**Section** a side-by-side display of many seismic traces.

**Seismic** the reflection seismology method commonly used to provide information about the subsurface structure of rock formations and the physical properties of both the subsurface rocks and the fluids within them.

**Seismic event** any continuous object on a seismic display.

**Seismic trace** a curve representing seismic attribute variation with time or depth at a specific (fixed) location. Usually is plotted with time (depth) increasing downward.

**Seismic wave** are energy wave that travels through the earth's layers. May be of natural (earthquake, volcanic eruption) or artificial origin (explosion, vibrator track).

**Shot** a seismic energy source.

**Signal-to-noise ratio** ratio of peak signal amplitude to average noise amplitude.

**Source** an object or process that generates seismic waves.

**Stack** the single output trace created by summing two or more input traces.

**Synthetic data** numerically created pseudo-seismic data used for testing processing algorithms or validating interpretation details.

**Synthetic seismogram** a simulated seismic trace (at a well location) based on sonic and density logs that is used to associate seismic reflections with geologic horizons.

**3-D seismic** the shooting and processing of seismic data in such a way that a cube of data is produced and interpreted for geologic meaning.

**3-D survey** a dense grid of parallel source lines (cross-line direction in this study) and receiver lines (in-line direction) established for seismic data acquisition and processing.

**Time slice** a horizontal display or view of 3-D seismic data having a certain arrival time.

**Time structure map** a map generated by tracking that displays vertical reflection time to a horizon of interest.

**Trace** a one-dimensional graph of a quantity vs. time or depth.

**Tracking** the interpretation process of following a reflection surface throughout a data volume and extracting the travel time to this surface.

**Velocity** the speed at which a seismic wave travels. Can vary from one location to another in the earth.

**Vertical resolution** the minimum separation of two features on a seismic trace that correspond to the top and base of a geologic unit or bed.

**Vertical seismic profile (VSP)** a seismic acquisition technique in which a surface source shoots into a series of receivers located down a well.

**Wavelength** the distance between successive equivalent points on two wave cycles.

**Zero offset VSP** a VSP that has one source, located at or near the wellhead.

## References

Biot MA (1962) Mechanics of deformation and acoustic propagation in porous media. J Appl Phys 33:1482–1498

Castagna JP, Sun S (2006) Comparison of spectral decomposition methods. First Break 24:75–79

Cluff RM, Cluff SG (2004) The origin of Jonah Field, northern Green River Basin, Wyoming. In: Robinson W, Shanley KW (eds) Jonah Field: case study of a giant tight-gas fluvial reservoir. American Association Petroleum Geologists Studies in Geology, p 127–145 (52, Chap. 8)

Dix CH (1955) Seismic velocities from surface measurements. Geophysics 20:68–86

Goloshubin G, Silin D (2006) Frequency-dependent seismic reflection from a permeable boundary in a fractured reservoir. Society of Exploration Geophysicists 2006 New Orleans annual meeting. Expanded abstracts 1742–1741

Goloshubin G, Silin D, Vingalov V, Takkand J, Latfullin M (2008) Reservoir permeability from seismic attribute analysis. Leading Edge 27:376–381

Kozlov K (2007) Seismic signature of a permeable, dual-porosity layer. Geophysics 72(5):SM281–SM291

Lindseth RO (1979) Synthetic sonic logs—a process for stratigraphic interpretation. Geophysics 44:3–26

Morlet J, Arens G, Fourgeau E, Giard D (1982) Wave propagation and sampling theory, Part II: sampling theory and complex waves. Geophysics 47:222–236

Neidell NS, Taner MT (1971) Semblance and other coherency measures for multichannel data. Geophysics 36:482–497

Partyka GA, Gridley J, Lopez J (1999) Interpretational applications of spectral decomposition in reservoir characterization. Leading Edge 18:353–360

Pride SR, Harris JM, Berryman JG, Yamomoto T, Wu R, Spetzler H, Rector JW, Nowack RL, Nihel KT, Mateeva A, Johnson DL, Fehler M (2003) Permeability dependence of seismic amplitudes. Leading Edge 22:518–525

Ren H, Goloshubin G, Hilterman FJ (2009) Poroelastic analysis of permeability effects in thinly layered porous media. Geophysics 74(6):N49–N54

Roberts A (2001) Curvature attributes and their application to 3-D interpreted horizons. First Break 19:85–99

Taner MT, Koehler F, Sheriff RE (1979) Complex seismic trace analysis. Geophysics 44:1041–1063